Available online at www.sciencedirect.com
SCIENCE DIRECT®
Geochimica et Cosmochimica Acta 70 (2006) 1821–1838
Geochimica
www.elsevier.com/locate/gca

Bubble growth in slightly supersaturated albite melt at constant pressure

Don R. Baker [a,*], Phyllis Lang [b], Geneviève Robert [a], Jean-Francois Bergevin [b], Emilie Allard [a], Liping Bai [a]

[a] Department of Earth and Planetary Sciences, McGill University, 3450 rue University, Montréal, Que., Canada H3A 2A7
[b] Department of Physics, McGill University, 3600 rue University, Montréal, Que., Canada H3A 2T8

Received 7 July 2005; accepted in revised form 11 January 2006

Abstract

Bubble growth experiments were performed in a piston-cylinder by hydrating albite melt with ~11 wt.% H_2O at 550 MPa followed by rapid decompression at 1 MPa s^{-1} to pressures of 450 or 400 MPa. At these conditions the melt was supersaturated with ~0.5 or ~1.5 wt.% H_2O, respectively, which caused rapid exsolution and bubble growth. Results at 1200 °C demonstrate that portions of the initial cumulative bubble-area distributions may be characterized by a power law with an exponent near 1, but they rapidly evolve to exponential distributions and approach a unimodal distribution after 32 h of growth. This evolution occurs by the growth of larger bubbles at the expense of smaller ones. The growth rate of the average bubble radius in these experiments is described by a power law whose exponent is 0.35, close to the theoretical exponent of 1/3 for phase growth in which coalescence is dominated by Ostwald ripening of the bubbles. Over the range of pressures and water contents investigated at 1200 °C, the bubble-size distributions and growth rate are not significantly affected by changes in the amount of exsolved water or by splitting the decompression path into two steps. Similar decompression experiments at 800 °C are dominated by smaller bubbles than in the 1200 °C experiments and also demonstrate exponential cumulative size distributions, but consistently contain a small fraction of larger bubbles. The growth rate of these bubble radii cannot be fit with a power law, but a logarithmic dependence of the bubble radii on time is possible, suggesting a difference in the growth mechanisms at low and high temperatures. This difference is attributed to the orders of magnitude changes in melt viscosity and water diffusion in the melt as the temperature varies from 800 to 1200 °C. At 1200 °C the transport properties of albite melt resemble those of natural basaltic melts whereas at 800 °C the properties are similar to those of andesitic to dacitic melts. The decompression rate used in this study exceeds natural rates by one to two orders of magnitude. Thus, these results indicate that natural mafic-to-intermediate magmas supersaturated with only a small excess of water should easily nucleate bubbles during ascent and that bubble growth in mafic magmas will proceed much more rapidly than in andesitic to dacitic magmas. Intermediate composition magmas also may be capable of forming bimodal bubble-size distributions even in the case when only one nucleation event occurred. The rapid evolution of the bubble-size distribution from a power law to an exponential may be useful in constraining the time duration between bubble nucleation and the quenching of natural samples.

1. Introduction

The exsolution of fluids from magmas and consequent vesiculation is the driving force of volcanic eruptions. The rate of exsolution and degassing controls the explosivity of an eruption; this rate is affected strongly by magma viscosity, volatile concentration, and the diffusion of dissolved volatiles (e.g., Sparks et al., 1994). If we can improve our understanding of bubble nucleation and growth, our understanding of volcanic processes will be enhanced significantly. In particular, knowledge of the distribution of bubble sizes, how it is formed, and how it affects the physical properties of magmas may provide a key we need to better predict volcanic eruptions.

Past studies of bubble nucleation and growth followed one of two different approaches. In one approach the researchers investigated bubble nucleation densities and

* Corresponding author. Fax: +1 514 398 4680.
E-mail address: donb@eps.mcgill.ca (D.R. Baker).

0016-7037/$ - see front matter © 2006 Elsevier Inc. All rights reserved.
doi:10.1016/j.gca.2006.01.011

bubble-size distributions in natural volcanic rocks. These researchers measured bubble-size distributions in natural lavas, which vesiculate on a time scale of seconds to hours, and pyroclastic materials, which vesiculate on a time scale of seconds. Some studies found that the bubble sizes in natural samples are described by exponential distributions (e.g. Toramaru, 1989, 1990; Klug and Cashman, 1996; Mangan and Cashman, 1996), whereas others found power-law distributions (e.g. Gaonac'h et al., 1996a, 2005; Klug et al., 2002). Much has been learned from studies of natural volcanic materials, however, important parameters such as the time for nucleation and growth and the viscosity of the melt during growth are often not well constrained, in part due to our lack of knowledge of the exact nature and timing of volcanic processes.

The other approach taken to study bubbles was to produce them in the laboratory under controlled conditions of pressure, temperature and time. We subdivide previous vesiculation experiments in two broad categories: (1) experiments in which volatile-bearing analogue melts, such as a mixture of gum rosin and acetone, are explosively decompressed from moderate to low pressures simulating volcanic eruptions (e.g. Mader et al., 1994; Blower et al., 2002); and (2) experiments where volatile-bearing silicic melts are first produced at high temperature and pressure conditions and then forced to vesiculate by dropping the pressure a few 10's to hundred's of megapascals over time periods of several minutes to several days to supersaturate the melt by several percent of H_2O and simulate ascent through a magmatic conduit (e.g. Hurwitz and Navon, 1994; Gardner et al., 1999; Simakin et al., 1999; Larsen and Gardner, 2000; Mangan and Sisson, 2000; Martel and Bureau, 2001; Mourtada-Bonnefoi and Laporte, 2002, 2004; Martel and Schmidt, 2003; Larsen et al., 2004; Mangan et al., 2004; Burgisser and Gardner, 2005). Most of these studies found a Gaussian distribution of bubble sizes, although notably Simakin et al. (1999) found a power-law distribution in a few of their experiments. This previous research has advanced our understanding of bubble nucleation and growth in igneous systems, but a comprehensive understanding of why bubble sizes follow a power law in some instances and an exponential distribution in others remains undiscovered.

2. Theories of bubble-size distributions

Cashman and Mangan (1994) and Mangan and Cashman (1996) applied earlier work on exponential crystal-size distributions by Marsh (1988) to vesicle-size distributions in volcanic rocks. A general mathematical form of a cumulative exponential size distribution is:

$$P(>A) \sim \exp(-BA), \tag{1}$$

where A is the area, $P(>A)$ is the probability of finding a bubble with an area larger than A and B is a constant. This theory is based upon the assumption of a steady state reservoir in which bubbles constantly nucleate, grow and leave the reservoir. Application of this model allows calculation of bubble nucleation and growth rates, with the caveat that the assumptions are fulfilled. Deviations away from the steady state theoretical prediction of an exponential distribution can be explained by coalescence, if too many large bubbles are present, and by Ostwald ripening, if too few small bubbles are present (Mangan and Cashman, 1996).

Two theories for power-law bubble-size distributions currently dominate the geological literature on the subject. This distribution has the general form:

$$P(>A) \sim A^{-N}, \tag{2}$$

where N, the cumulative, or integrated, area exponent, is the absolute value of slope of the line describing the distribution on a log–log plot. The first power-law theory for bubble sizes was introduced by Gaonac'h et al. (1996b) and expanded by Lovejoy et al. (2004), in which the presence of a power-law bubble-size distribution is explained by diffusive growth of small bubbles and a cascading series of binary collisions between bubbles. At each generation two bubbles coalesce into a single larger bubble and with each succeeding generation the size of the coalescing bubbles increases. The predicted cumulative area power-law exponent for this model is 1 (which corresponds to an cumulative power-law exponent of 2 for the radii distribution), and the authors provide details on how this value can be modified to slightly lower values, ~0.8, by other mechanisms. With time, coalescence of the largest bubbles leads to a higher-valued exponent once the supply of smaller bubbles is exhausted, and the distribution can evolve into a distribution described by an exponential function. Gaonac'h and coworkers (Gaonac'h et al., 1996a, 2005) measured the bubble-size distributions in lavas and pumices produced in plinian eruptions and demonstrated that the observed size distributions agreed with their theoretical power-law distribution.

The second model for power-law distributions by Blower et al. (2001, 2002) is based upon Apollonian closest-packing resulting from multiple nucleation events. Blower et al. (2002) used simulations to support their hypothesis and found that typically after ~3 nucleation events an exponential bubble-size distribution was created and that after only ~5 nucleation events power-law size distributions begin to evolve. Blower et al.'s (2002) simulations demonstrated that the power-law exponent of the bubble-size distribution increased as the number of nucleation events increased, but appeared to asymptotically approach a value of 2.5 for the radius, which when converted into the cumulative area exponent of this study is equivalent to 0.75. This exponent calculated by Blower et al. (2002) is within error of the measurements they made on analogue melts and the results of Gaonac'h et al. (1996a,b).

Two other theories applicable to bubble-size distributions not commonly discussed in the geological literature also deserve exposition. The first of these theories is that Buldyrev et al. (2003) proposed for systems in which

resources from a large region, or a basin of attraction, are concentrated into a smaller region; a physical rationalization of this concept is that if bubbles nucleate far apart from one another they grow in large basins of attraction, whereas if bubbles nucleate close together their basins are small. Starting with the assumption that the size of the bubbles, V, is proportional to the volume of the basin of attraction and that there are many sizes of basins, each consisting of z subdivisions, Buldyrev et al. (2003) demonstrate that the size of the bubbles is proportional to z^{-n} and that number of bubbles in the size fraction between z^{-n} and z^{-n-1} scales as V^{-2}. Converting the volume exponent of 2 in the Buldyrev et al. model into the cumulative area exponent of our study (following Gaonac'h et al., 1996a,b) yields an exponent of 1, similar to the values predicted by Gaonac'h et al. (1996a,b) and Blower et al. (2002).

The last theory to describe a power-law distribution is designed for the filling of space. Dodds and Weitz (2002) numerically investigated several models for the distribution of radii of randomly sized spheres which fill three-dimensional space. Dodds and Weitz found that the distribution of the sphere radii followed a power law with an exponent of 3.7, which when converted into the cumulative area exponent used in our study yields 0.85, once again within measurement error of the exponents predicted by the other theories of bubble growth. Although this model may be useful in the understanding of highly vesicular rocks and polydisperse foams, such as those studied by Blower et al. (2002), only one of our experiments has a vesicularity great enough for the bubbles to approach a space-filling foam.

Each of these models relies upon different mechanisms to explain the power-law distribution of bubble sizes, but yet they each predict a cumulative area exponent near 1.0. The goal of our experimental study was to investigate the evolution of the bubble-size distribution formed by the exsolution of small amounts of water from a silicate melt. Because many different processes can theoretically produce power-law distributions of bubble sizes, at the outset of this study we expected to find a power-law distribution and to see the evolution of bubble sizes from a distribution characterized by small bubbles of similar size formed soon after nucleation and early growth, to larger bubbles displaying a power-law distribution with an exponent near 1.0 at intermediate times, and then to distributions with increasingly larger power-law exponents.

In this report, we present the results of our investigation of the evolution of the bubble-size distribution during the vesiculation of a melt slightly supersaturated with water at moderate pressures. In contrast to previous studies, we wished to investigate the formation and growth of bubbles in silicate melts at conditions of small supersaturation, near 1 wt.% H_2O. The rationale for investigating bubble growth under slightly supersaturated conditions was to simulate small amounts of degassing in magma conduits at middle-to-upper crustal depths and to compare our results with the previous ones obtained at high supersaturation and lower pressures. We chose to study albite melt as an analogue composition for natural melts because of its well-characterized properties.

3. Experimental techniques

3.1. Albite glass synthesis

The albite glass used in the experiments was made from a mixture of SiO_2, Al_2O_3, and Na_2CO_3. Appropriate amounts of these oxides and the carbonate were ground together in an agate mortar under alcohol for 1 h. The mixture was placed in a platinum crucible, decarbonated at 1000 °C for 8 h and then melted twice at 1575 °C for 2 h with intermediate crushing and grinding. This glass was crushed and ground again followed by an additional 6 h of melting at 1575 °C. With the exception of a few chips saved for microprobe analysis, this glass was crushed, ground and sieved to produce a powder between 38 and 45 μm and stored at 110 °C.

Electron microprobe analysis of this starting material used albite as the standard for Na, orthoclase for K, Al, and Si, and andradite for Fe. A 15 kV accelerating voltage with a 5 nA beam of either 10 or 20 μm in diameter was used for analysis. Based upon 16 analyses of the starting glass, the concentrations of potassium and iron were below electron microprobe detection limits and the composition of the albite glass is $Na_{0.97}Al_{1.00}Si_{3.03}O_8$ (Table 1).

3.2. Vesiculation protocol

We performed vesiculation experiments in a piston-cylinder apparatus at 400 and 450 MPa using 19.1 mm NaCl–pyrex–crushable alumina assemblies and a hot piston-in procedure (Baker, 2004). We filled $Au_{75}Pd_{25}$ capsules of 3 mm O.D. with approximately 2.7 mg distilled and deionized water and approximately 22 mg of albite glass powder to produce experiments with approximately 11 wt.% water. This water concentration is ~0.5 wt.% below the saturation value at 500 MPa, but slightly supersaturated at 450 MPa, where saturation occurs at 10.5 wt.% and the supersaturation pressure is 25 MPa, and more supersaturated at 400 MPa, where saturation occurs at 9.4 wt.% and the supersaturation pressure is 75 MPa (Behrens et al., 2001). Capsules were welded without volatile loss and then stored in a 110 °C oven for at least 2 h to homogenize water in the capsule. In many cases two identical capsules were put into the same assembly to duplicate each experiment, but occasionally one capsule was lost during the run. We surrounded all capsules with pyrophyllite to minimize water loss from the melt to the assembly. We calibrated our assemblies against the melting temperature of NaCl at 920 °C, 500 MPa (Bohlen, 1984) and determined the need for a 50 MPa correction to the nominal pressure; this pressure correction was also checked by measuring the water solubility in some of the run products of this study using the "difference from 100" electron microprobe technique (Baker, 2004). Pressure was within 16 MPa of the desired pressure during the experiments. Temperatures were measured with type C, tungsten–rhenium thermocouples and controlled to within 3 °C of the set point.

To begin each experiment we simultaneously pressurized and heated it to 550 MPa, 1200 °C and held it at those conditions for 1 h, which we

Table 1
Electron microprobe analysis of starting albite glass

Oxide	Albite glass (wt.%)	Ideal albite (wt.%)
SiO_2	69.20 ± 0.45[a]	68.74
Al_2O_3	19.32 ± 0.13	19.44
Na_2O	11.36 ± 0.11	11.82
Total	99.88	100.00

[a] Uncertainties correspond to 1 standard deviation about the mean based upon analysis of 16 random spots of the glass.

calculated to be far in excess of the time necessary for water to diffuse into the albite melt based upon the measurements of Behrens and Nowak (1997). After this first hour the pressure was reduced to either 450 or 400 MPa at a rate of approximately 1 MPa s^{-1} and then held at the desired pressure for durations from 0 to 32 h (Table 2) to allow bubble growth, which was terminated by isobaric quenching.

Most experiments were performed at 1200 °C where the viscosity of albite melt is approximately 20 Pa s (estimated from the results of Dingwell, 1987) and the diffusion coefficient for water in the melt is between 0.6 and 11×10^{-11} m^2 s^{-1} (Behrens and Nowak, 1997). We performed a few experiments by decreasing the temperature to 800 °C before depressurization to 450 MPa to investigate the effects of changing melt viscosity and water diffusion on bubble growth. At this temperature water solubility remains at 10.5 wt.% (Behrens et al., 2001); the viscosity of the melt is approximately 9000 Pa s (estimated from Dingwell, 1987), and the diffusion coefficient of water is between 0.3 and 4×10^{-13} m^2 s^{-1} (estimated from Behrens and Nowak, 1997).

One set of experiments was performed to investigate if two-step depressurization, which might lead to multiple nucleation events, affects the bubble-size distribution. In these experiments the sample was first melted at 1200 °C, 550 MPa for 1 h. Then, the sample was depressurized to 450 MPa and held at that pressure and 1200 °C for 2 h; this step was followed by a second depressurization to 400 MPa and the sample was held at this pressure and 1200 °C for 8 h.

For comparison with the high pressure experiments, in which only a small amount of water exsolved from the melt, one experiment was performed by hydrating the melt with 10.9 wt.% H_2O at 1100 °C, 550 MPa, for 1 h followed by isobaric quenching. The glass was removed from the capsule and put into a small furnace at 1 atm and heated in air to 750 °C over a duration of 15 min during which exsolution and bubble growth occurred. The water diffusion coefficient and the viscosity of this sample change by orders of magnitude during degassing as the water-rich sample was heated from room temperature to 750 °C and lost water into the growing bubbles. We can estimate a maximum water diffusion coefficient and a minimum viscosity similar to that seen in the 800 °C, 450 MPa experiments, or 0.3 to 4×10^{-13} m^2 s^{-1} and 9000 Pa s, respectively. At the opposite extreme, after virtually all the water has exsolved from the melt, the water diffusion coefficient is probably near 2×10^{-14} m^2 s^{-1}

Table 2
Bubble growth experiments

Expt.	Temperature (°C)	Pressure[a] (MPa)	Time[b] (h)	V[c] (%)	r[d] (μm)	N_d[e] (cm^{-3})	S[f] (μm)	H_2O[g] (wt.%)	Exsolved H_2O[h] (wt.%)
AB-2	1200	550	1	1.6	0.64 (0.12)	3.5×10^6	41	11.1	0
AB-4	1200	550/450	1/0	2.8	0.76 (0.21)	6.7×10^6	33	10.9	0.4
AB-11	1200	550/450	1/0.5	5.8	1.13 (0.42)	8.3×10^6	31	10.7	0.2
AB-12	1200	550/450	1/0.5	8.1	2.01 (1.12)	9.7×10^6	29	11.1	0.6
AB-13	1200	550/450	1/2	7.3	1.64 (0.36)	4.5×10^6	38	11.1	0.6
AB-14	1200	550/450	1/2	6.6	4.93 (1.11)	0.9×10^6	64	11.0	0.5
AB-15	1200	550/450	1/8	7.4	5.50 (1.15)	3.1×10^6	43	10.9	0.4
AB-16	1200	550/450	1/8	6.7	3.65 (0.92)	3.8×10^6	40	11.1	0.6
AB-18	1200	550/450	1/32	6.0	6.09 (1.08)	4.6×10^6	37	11.0	0.5
AB-19[i]	1200/800	550/450	1/2	4.5	1.44 (0.44)	8.1×10^6	31	11.7	1.2
AB-20[i]	1200/800	550/450	1/2	4.3	n.r.	7.4×10^6	32	11.0	0.5
AB-21[i]	1200/800	550/450	1/32	1.7	1.39 (0.45)	3.8×10^6	40	11.2	0.7
AB-22[i]	1200/800	550/450	1/32	4.6	0.66 (0.49)	1.5×10^7	25	11.2	0.7
AB-27	1200	550/400	1/2	1.4[j]	2.73 (0.87)	1.8×10^6	51	11.0	1.6
AB-29	1200	550/400	1/8	5.7	2.14 (0.68)	1.3×10^7	26	11.1	1.7
AB-37	1200	550/450/400	1/2/8	6.8	3.46 (1.52)	6.5×10^6	33	10.8	1.4
AB-38	1200	550/450/400	1/2/8	7.0	4.42 (2.29)	6.7×10^6	33	10.9	1.5
AB-24	1100/750	550/0.1	1/0.25	22.4[k]	n.r.	5.8×10^6	35	10.9	10.9

[a] Nominal pressure + 50 MPa, based upon calibration with NaCl melting at 500 MPa, 920 °C and measured water solubility in the albite melt (Baker, 2004).

[b] The duration of the experiment at each pressure is given if the form X/Y, where X is the duration at the higher pressure and Y is the duration at the lower pressure.

[c] V is the two dimensional vesicularity as measured from backscattered images of the run products. Note that vesicles occasionally found along capsule walls are not included in this estimate.

[d] Mean radius of bubbles totally enclosed by melt followed by 1-sigma standard deviation in parentheses. These data were determined by fitting a Gaussian curve to the distribution of three-dimensional bubble radii (calculated following Sahagian and Proussevitch, 1998) and ignoring bubbles formed during quenching. Note that for AB-4, the zero-time experiment, all bubbles were used to determine the mean radius and that for AB-20 and AB-24 the averages are negative numbers and are not reported ("n.r." in table).

[e] N_d is the three-dimensional number density of bubbles, which is calculated from the sum of the density distribution of bubble radii (Fig. 13). N_d is expressed in number of bubbles per cm^3 of the total sample (glass + bubbles) for comparison with previous studies.

[f] S is the average spacing between bubbles calculated from the three-dimensional number density: $S = (3/(4\pi N_d))^{1/3}$ (see Lyakhovsky et al., 1996).

[g] Concentration of water initially added to the experiment. The water solubility in albite melt at 550 MPa is 13 wt.%, at 450 MPa is 10.5 wt.%, and at 400 MPa is 9.4 wt.% (Behrens et al., 2001).

[h] The difference between the water solubility in albite melt at the conditions studied and the initial amount of water dissolved in the melt. Selected experiments were analyzed with the electron microprobe and the "difference from 100" technique was used to measure the dissolved water in glass (see Baker, 2004 for further details).

[i] Experiments AB-19, AB-20, AB-21 and AB-22 were hydrated at 550 MPa, 1200 °C, then the temperature was lowered to 800 °C before dropping the pressure to 450 MPa.

[j] Only a small portion of this sample was recovered and this vesicularity is considered to be anomalously low due to poor sampling statistics.

[k] Vesicularity varied from 9% to 43% and was extremely heterogeneous, even in neighboring images.

(estimated from Shaw, 1974) and the viscosity is near 10^{11} Pa s (Webb and Knoche, 1996).

3.3. Analysis techniques

Run product capsules were mounted in epoxy, ground, and polished to a 0.3 μm finish for analysis of the bubble-size distribution through backscattered electron (BSE) imaging on an electron microprobe (Fig. 1). Bubble-size distributions in the images were analyzed using the ImageJ software package (Rasband, 1997–2005; Abramoff et al., 2004) by thresholding the images to make them binary black (vesicles) and white (glass) images and then using the particle counting routine to measure the area of each vesicle. Bubble areas were converted into radii of equivalent area circles and these radii converted into three dimensions following the techniques of Sahagian and Proussevitch (1998). For all but two experiments we collected enough images, approximately 15, to measure the areas of a minimum of 400 bubbles for the determination of the size distribution; in most cases we measured in excess of 1000 bubbles. With the exception of experiment AB-2, all images were collected at 400× magnification which produced an analyzed area of approximately 276×183 μm^2 in each image; images of experiment AB-2 were collected at 600× because of the small bubble sizes in this experiment.

Although large bubbles were occasionally observed at the interface between the quenched melt and both the radial and end walls of the capsule, only bubbles that were completely surrounded by quenched melt were measured. This procedure was followed because of our inability to determine whether the large bubbles at the melt–capsule wall interface were formed by heterogeneous nucleation at the interface or by another mechanism, and because they did not display circular cross-sections which makes accurate measurement from two-dimension imaging impracticable. A few of these bubbles were quite large, with areas greater than 1000 μm^2, but the numbers of such large bubbles were so low that even if we could accurately measure their sizes and fit a function to their distribution, the statistical validity of the fit would be questionable.

3.4. Treatment of the measurements and their uncertainties

Following Gaonac'h et al. (1996a,b), Blower et al. (2002) and Hergarten (2002), we plot the probability of finding a bubble greater than a given area against the area class (Figs. 2–12) on log–log plots. These plots correspond to the cumulative, or integrated, areas of the bubbles. Power-law size distributions are easily detected on these plots because the data form a straight line (Hergarten, 2002); such a power law is characterized by its exponent, in this case the cumulative area exponent (Eq. (2)). If the bubble-size distribution forms a curved array on this type of plot, the distribution may be characterized by an exponential function (Eq. (1)). Bubble-size distributions that create a horizontal line indicate a unimodal size distribution.

The uncertainties in the number of bubbles falling into each size class follow Poisson statistics and scale as the square root of the number of bubbles, thus when 1000 bubbles are counted the uncertainty bars in the figures are smaller than the data points except when the probability of a size class is less than 0.01; when the probability falls to 0.001 the uncertainty reaches a maximum of approximately 3 times the size of the data points in the figures. Exponential functions were typically fit to all size classes with a probability in excess of 0.01, and power-law functions were fit to size classes that appeared to follow linear trends on the plots and also had a probability greater than 0.01.

The uncertainties in the power-law exponents and the exponential coefficients were calculated by a Monte Carlo technique based upon the number of bubbles in each of the size classes in experiments AB-4 (1048 bubbles counted), AB-27 (200 bubbles) and AB-29 (3096 bubbles). The number of bubbles in each size class was modified by randomly adding or subtracting a random fraction of the Poisson uncertainty to the number of

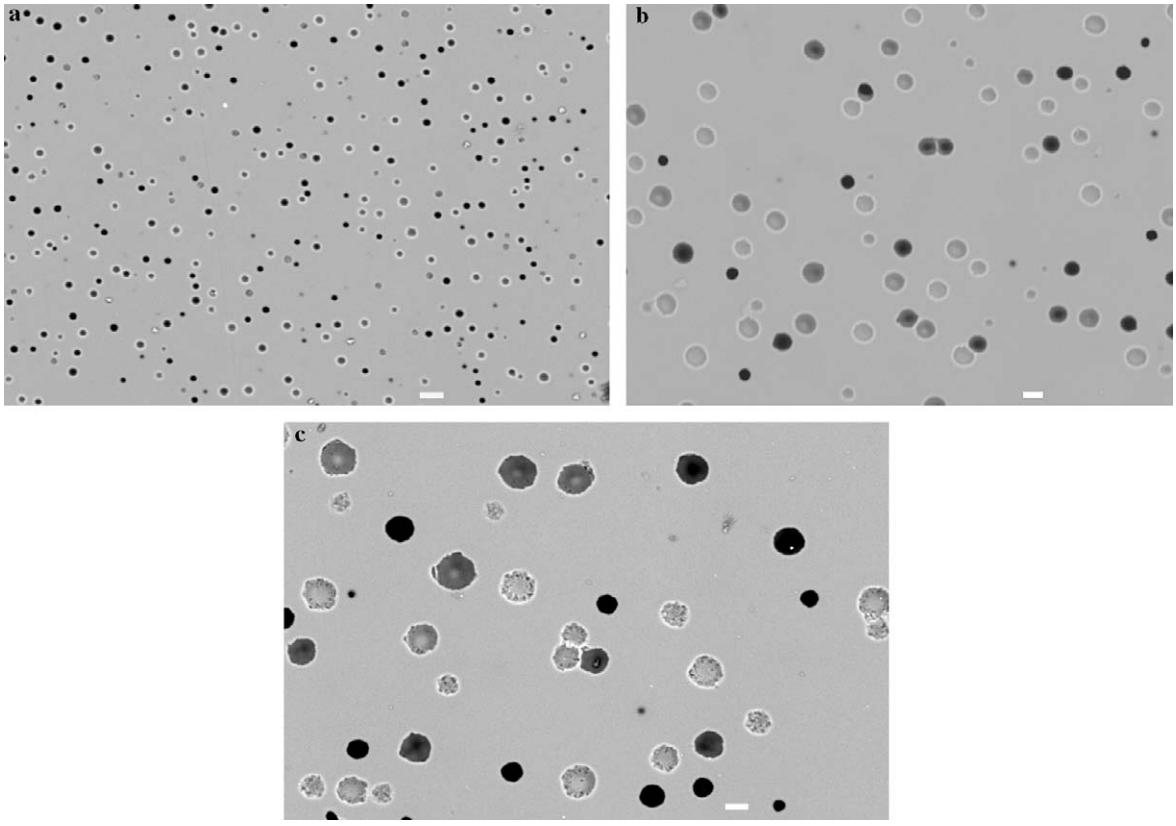

Fig. 1. The growth of bubbles with increasing experimental duration. Backscattered electron (BSE) images of 3 experiments performed at 450 MPa, 1200 °C. (a) AB-12, 0.5 h duration, (b) AB-13, 2 h duration, (c) AB-18, 32 h duration. Each image was obtained at 400x magnification, and the white scale bar is 10 μm in length.

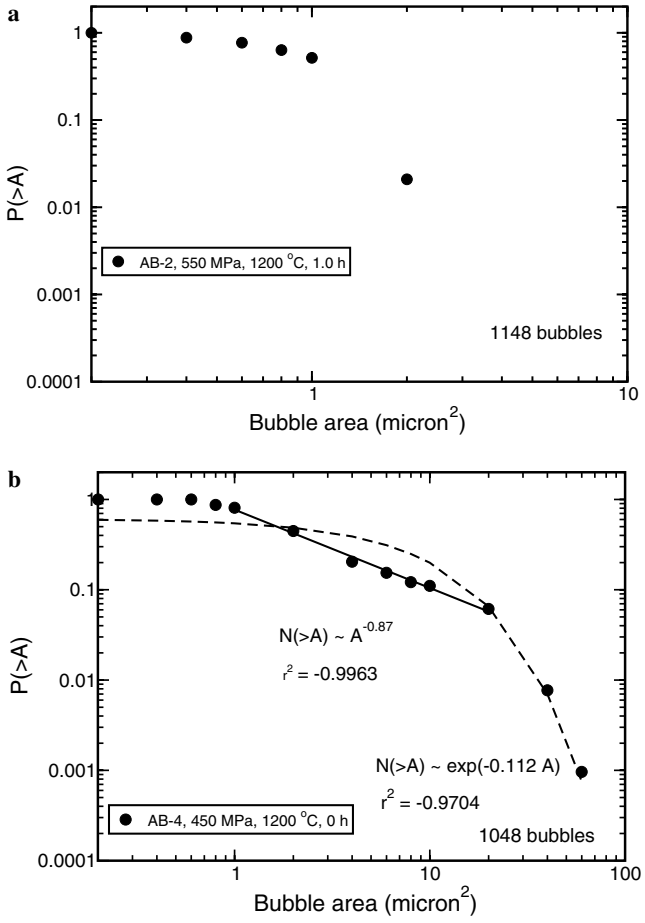

Fig. 2. Cumulative bubble-size distributions measured from BSE images for: (a) experiment AB-2 which was isobarically quenched after 1 h at 550 MPa where it was water-undersaturated and demonstrates the formation of quench bubbles, and (b) experiment AB-4 which was isobarically quenched immediately upon reaching the final pressure of 450 MPa where it was 0.4% supersaturated with water. The presence of bubbles demonstrates the ease of bubble nucleation in the experiments. In these and the following figures (2–12) the abscissa is the area class of the bubbles and the ordinate is the probability of finding a bubble whose area exceeds the specified area class. Note that each panel provides the number of bubbles counted for the determination of the probability. Also shown in panel b and in subsequent figures are the exponential fit to the data (the dashed line) and the power-law fit to the portion of the data that appears linear on these log–log plots (the solid line). Complete explanations of the fits and uncertainties are given in the text.

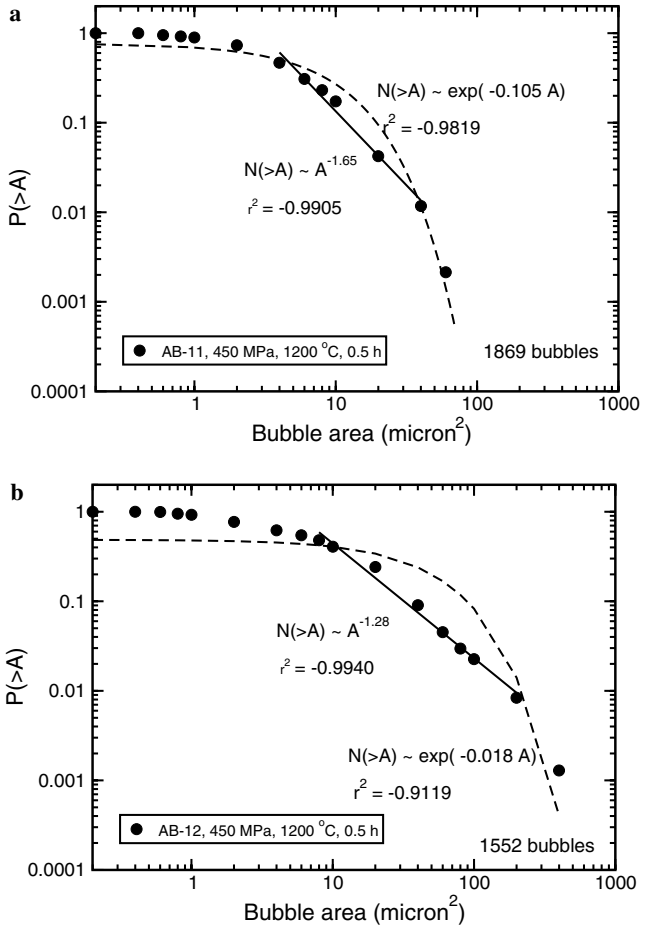

Fig. 3. Cumulative bubble-size distributions measured from BSE images for: (a) experiment AB-11 and (b) experiment AB-12, both of which were performed for 0.5 h at 1200 °C, 450 MPa. Note the presence of power-law regions in each of these figures for bubbles in size classes between ~10 and ~100 μm² and the poor fit of exponential functions to the data.

counted bubbles. This procedure was repeated 10 times to create 10 surrogate data sets and then the data sets were fit with the same techniques used for the experimental measurements. Based upon the two-sigma standard deviations of these 10 data sets, the uncertainty in the exponent of the power-law fits is approximately 0.04 for AB-4 and AB-29, and 0.2 for AB-27. Using the same technique to calculate the uncertainty in the coefficients of the exponential fits yields an uncertainty of 0.002 for AB-29, 0.02 for AB-4, and 0.006 for AB-27.

4. Experimental results

4.1. General observations

All experiments produced bubbles distributed throughout the quenched melt and at the melt–capsule interface. The number density of bubbles in the experiments varies by only an order of magnitude from $\sim 1 \times 10^6$ to $\sim 2 \times 10^7$ bubbles per cm^3 (Table 2) and these number densities can be converted to average inter-bubble spacings of between 25 and 64 μm (Table 2). Depending upon the experiment, the bubble areas varied from less than 1 μm^2 to in excess of 100 μm^2. When converted into three-dimensional radii the average bubble radii range from less than 1 μm in the shortest experiments to 6 μm in one of the longest ones. In none of the samples were crystals observed and electron microprobe analysis of selected runs demonstrated that the chemical composition and water concentration of the glass were homogeneous (see Baker, 2004). An example of the development of the bubble-size distribution at 1200 °C, 450 MPa is shown in Fig. 1 where back-scattered electron images from an experimental time series is presented. The images demonstrate the rapid formation of bubbles in the 0.5 h experiment followed by their slow maturity to the bubble sizes seen in the 32 h experiment. These images qualitatively portray the bubble size evolution; using our quantitative measurements and analysis we can statistically

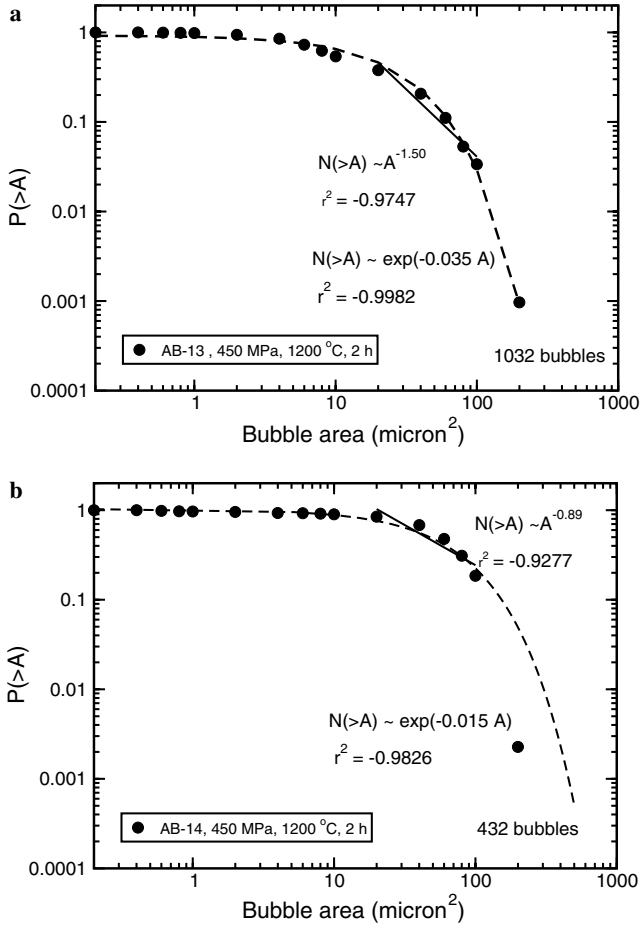

Fig. 4. Cumulative bubble-size distributions measured from BSE images for: (a) AB-13 and (b) AB-14, both performed for 2 h at 450 MPa, 1200 °C. The power-law fits in these experiments are in the same range of size classes as in Fig. 3, but the data are better fit by exponential functions.

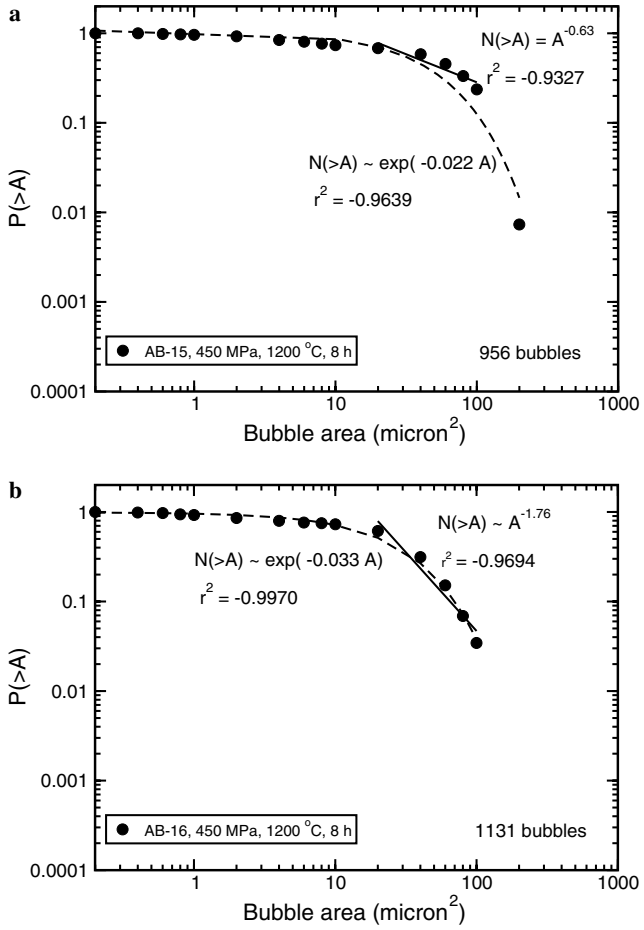

Fig. 5. Cumulative bubble-size distributions measured from BSE images for: (a) AB-15 and (b) AB-16, 8 h experiments at 450 MPa, 1200 °C. As in Fig. 4, the exponential fits to the complete data set are better than the power-law fits over the size classes of ~10 to ~100 μm^2.

compare the results of different experiments with one another and investigate the development of the bubble-size distributions.

4.2. Zero-time experiments

Experiments AB-2 and AB-4 were performed to determine the initial conditions during vesiculation. Experiment AB-2 was quenched immediately after 1 h at 1200 °C, 550 MPa (Fig. 2a). At these conditions it should be water-undersaturated, but it contained 1.6% vesicles, which we interpret to have formed during the quench. The quench bubbles indicate that nucleation occurs without a measurable delay in this melt at the conditions studied. The maximum bubble size in this experiment is only a few square microns; we found no large bubbles indicative of trapped intergranular gases as seen in low pressure experiments (e.g. Gardner et al., 1999). Experiment AB-4 is a zero-time experiment that was melted for 1 h at 1200 °C, 550 MPa and then depressurized to 450 MPa and immediately quenched (Fig. 2b). The bubble-size distribution is much broader in this experiment, and compared to AB-2 the

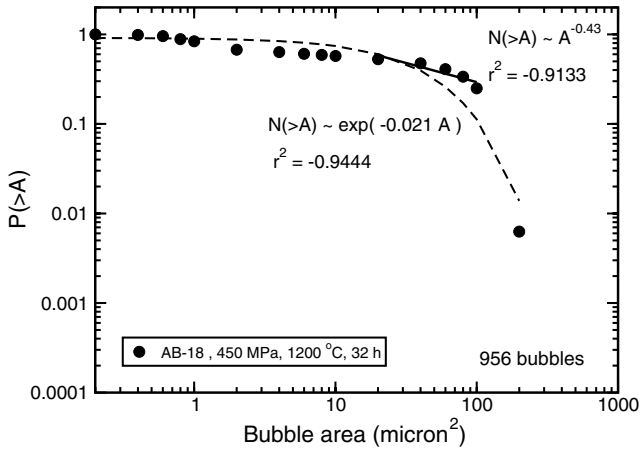

Fig. 6. Cumulative bubble-size distributions measured from BSE images for AB-18, which was held at 450 MPa, 1200 °C for 32 h. The probability of finding a bubble greater than a specific size is almost a horizontal line up to the size class of 100 μm^2, beyond which the probability falls drastically. This shape is similar to that of a unimodal size distribution, which would plot as a horizontal line up to the size followed by a drop to zero probability above that size.

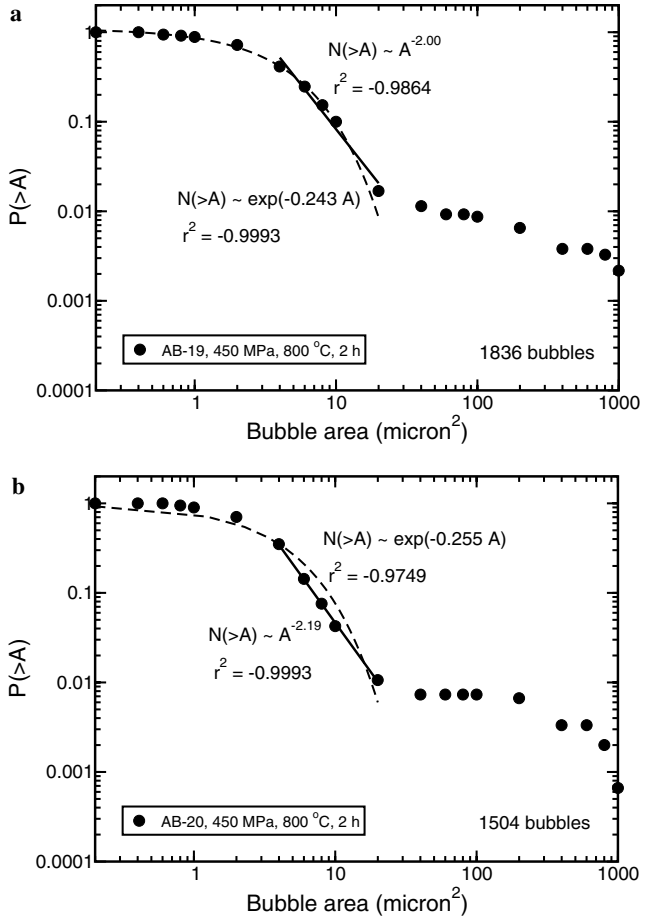

Fig. 7. Cumulative bubble-size distributions measured from BSE images for: (a) AB-19 and (b) AB-20. These experiments were performed at 450 MPa, 800 °C for 2 h and demonstrate that most bubbles fall into size classes less than 10 μm^2, much smaller than the bubbles produced in the 1200 °C experiments at the same pressure. The bubble-size distribution for the small bubbles is fit well by an exponential function, but a power-law function is also a suitable description of the data. The nearly horizontal tail of larger bubbles, reaching size classes of 1000 μm^2, also distinguishes these 800 °C experiments from the higher temperature ones; the number of bubbles in these tails is too small for a reliable fit.

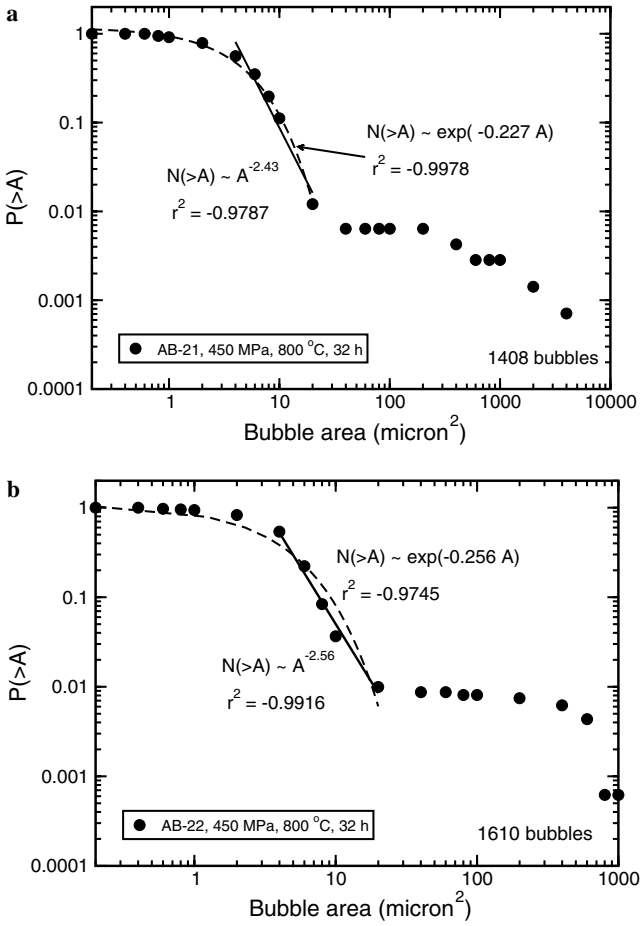

Fig. 8. Cumulative bubble-size distributions measured from BSE images for: (a) AB-21 and (b) AB-22, which are 32 h duration experiments at 800 °C, 450 MPa. The cumulative size distributions in these experiments are almost identical to those in the 2 h experiments shown in Fig. 7.

maximum bubble size is almost 2 orders of magnitude larger, indicative of water saturation. The larger bubble sizes seen in AB-4 compared to AB-2 indicate that even when the melt is only slightly supersaturated bubbles grow rapidly at the conditions investigated. The bubble-size distribution in AB-4 can be fit with a power law for bubbles between 1 and 20 μm^2 in area, which has an exponent of ~0.9; in contrast, the exponential fit to the entire distribution is much poorer (Fig. 2b).

4.3. Single-step decompression to 450 MPa

Experiments were performed for increasing duration at 450 MPa. The experiments AB-11, -12, -13, -14, -15, -16, and -18 (Figs. 3–6) demonstrate that with longer duration the fraction of bubbles in the range of approximately 10–100 μm^2 increases, but the maximum size of the bubbles

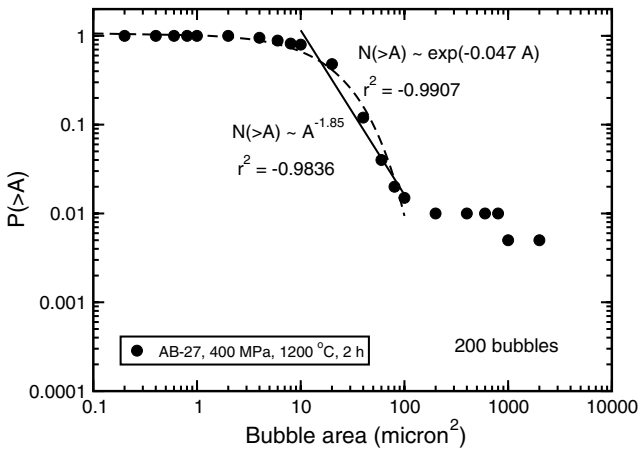

Fig. 9. Cumulative bubble-size distributions measured from BSE images for AB-27, which was performed at 400 MPa, 1200 °C, for 2 h. Most of this sample was lost during polishing reducing the number of bubbles counted and the reliability of the data.

remains approximately constant. A range of bubble sizes in the 0.5 h experiments, AB-11 and AB-12, can be fit with power laws (Fig. 3). An exponential fit also describes the

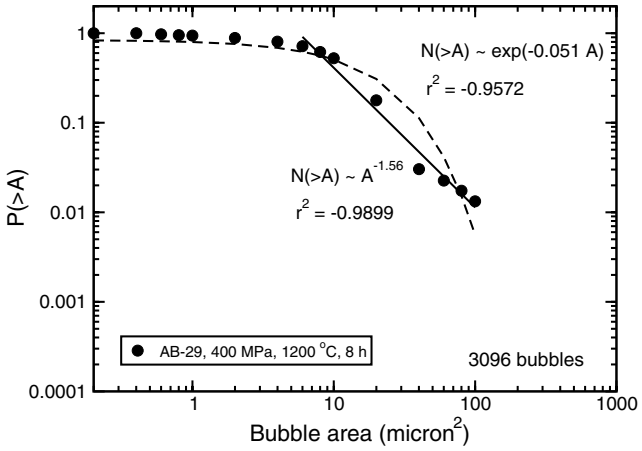

Fig. 10. Cumulative bubble-size distributions measured from BSE images for AB-29, which was performed at 400 MPa, 1200 °C, for 8 h. Although the power-law fit to the data is excellent, note that only 1 data point, for the size class 40 μm^2 falls off of the exponential fit.

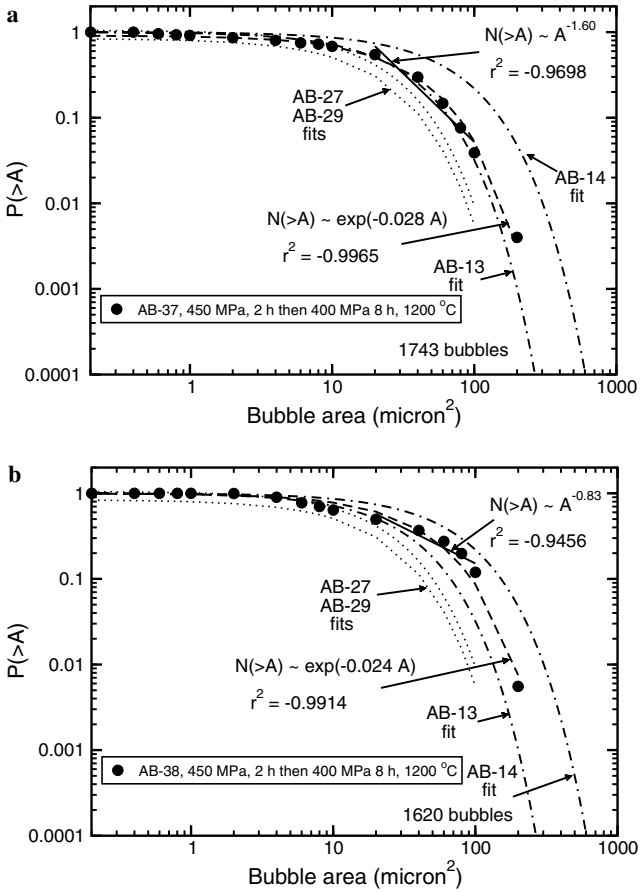

Fig. 11. Cumulative bubble-size distributions measured from BSE images for: (a) AB-37 and (b) AB-38. These are two-step experiments at 1200 °C which were decompressed to 450 MPa and held there for 2 h and followed by decompression to 400 MPa and maintenance at that pressure for 8 h. The data are excellently fit by exponential functions. Also plotted on these diagrams are the exponential fits to the single-step experiments at 400 MPa, 1200 °C, AB-27 and AB-29, and the single-step experiments which were held at 450 MPa for 2 h, AB-13 and AB-14. The distributions of the latter pair reflect the expected bubble-size distributions in AB-37 and AB-38 at the end of the first decompression step at 450 MPa.

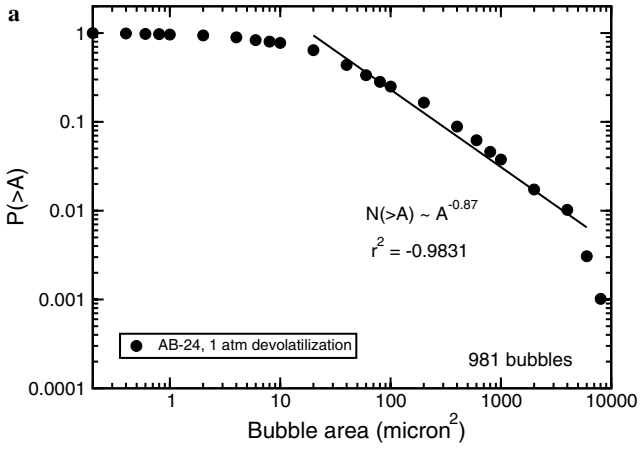

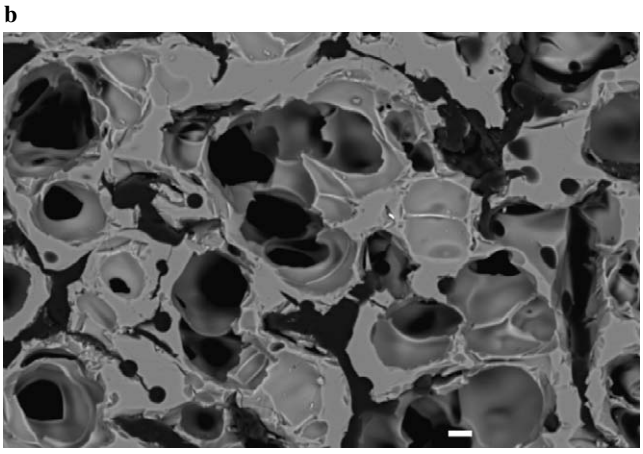

Fig. 12. (a) Cumulative bubble-size distribution measured from BSE images of AB-24. This sample was hydrated at 550 MPa, 1100 °C and quenched to ambient conditions. A chip of this glass was heated at 1 bar pressure to 750 °C over a 15 min duration and allowed to foam and release virtually all of the 10.9 wt.% H_2O dissolved into the melt during hydration. The bubble sizes cover a similar range as the high pressure experiments but clearly follow a power-law, not an exponential, distribution. (b) BSE image of AB-24 taken at 400× demonstrating the coalescence of bubbles and the foamy nature of the sample; the scale bar is 10 μm long.

entire set of measured bubble sizes in AB-11, but in AB-12 an exponential function does not suitably describe the distribution. All longer experiments, AB-13 and AB-14 of 2 h duration (Fig. 4), AB-15 and AB-16 of 8 h duration (Fig. 5), and AB-18 of 32 h duration (Fig. 6), contain bubble-size distributions better fit by exponentials than by power laws, but note that the 32 h experiment (AB-18) can almost be described by a unimodal size distribution.

The experiments performed at 800 °C, 450 MPa (Figs. 7 and 8) contain smaller bubbles, most are below the 20 μm^2 size class. When we consider bubbles 20 μm^2 or less, the bubble-size distributions in the 2 h experiments (AB-19 and AB-20, Fig. 7) can be fit with either an exponential function or, over the size range of 4–20 μm^2 with a power law containing an average exponent of ~2.1. The 32 h experiments (AB-21 and AB-22, Fig. 8) also can be fit with an exponential, or over the same size ranges as used in AB-19 and AB-20 with a power law whose average

exponent is ~2.5. An exponential distribution is a more accurate description of the bubble-size distribution in these experiments, similar to the 450 MPa, 1200 °C experiments. Although most of the bubbles are less than 20 μm^2 in area, each experiment contains a small fraction of bubbles, less than 1%, with sizes between 40 and ~1000 μm^2. These larger bubbles follow either a flat or possibly a power-law distribution. Unfortunately, the number of large bubbles seen in these experiments is too small to reliably fit with either an exponential or a power-law function and thus such functions for the large bubbles are not plotted in the figures.

4.4. Single-step decompression to 400 MPa

Experiments at 1200 °C, 400 MPa (AB-27 and AB-29) behave similarly to those performed at 1200 °C and 450 MPa. Most of the bubbles in the 2 h experiment, AB-27, can be fit with either an exponential function or a power-law function containing an exponent of ~1.9 (Fig. 9), slightly larger than the power-law exponent found at 450 MPa after the same duration, 1.5 (Fig. 4). Experiment AB-27 at 400 MPa contains two (2) large bubbles, which were not seen in the corresponding 2 h experiment at 450 MPa.

The power law describing the bubble sizes in the 8 h experiment at 400 MPa, AB-29 (Fig. 10), appears more evident than in the 8 h, 450 MPa experiments, AB-15 and AB-16 (Fig. 5), because it spans a larger size range of bubbles, from 7 to 100 μm^2 instead of 40 to 100 μm^2 (Fig. 5). However, with the exception of the point for bubbles with an area greater than 40 μm^2, the bubble-size distribution can also be fit well by an exponential. The exponent of the power-law distribution for this 8 h, 400 MPa experiment is ~1.6 (Fig. 10), whereas the power law determined for the 8 h, 450 MPa experiments has an average exponent of ~1.2.

4.5. Two-step decompression to 400 MPa

Two-step decompression experiments were performed to investigate the possibility of multiple nucleation events and their effect on the bubble-size distribution. Experiments AB-37 and AB-38 were performed by decompression to 450 MPa and maintenance of that pressure for 2 h followed by decompression to 400 MPa where they were held for 8 h (Fig. 11). At the end of the first 2-h step at 450 MPa the bubble-size distribution in each of these experiments should have resembled those measured in the single-step decompression experiments AB-13 and AB-14 (Fig. 4).

These experiments demonstrate that the two-step decompression path may result in the growth of slightly larger bubbles than those seen in the single-step decompression experiments to 400 MPa. The bubble-size distributions in AB-37 are well explained by a power law with an exponent of 1.8 over the range of 20–100 μm^2, but an exponential curve is also an excellent fit to all of the measurements. Bubble sizes between 20 and 100 μm^2 in AB-38 can be fit with a power law whose exponent is 0.83, and the entire distribution also is fit excellently by an exponential function. Although both AB-37 and AB-38 contain bubble-size distributions plotting at higher probabilities for large bubbles when compared to single-step experiments AB-27 and AB-29, these distributions are below that in the single-step decompression experiment AB-14 at 450 MPa; this is attributed to the stochastic nature of bubble growth in these experiments. These experiments demonstrate that separating the decompression into two steps has little or no effect on the bubble-size distribution.

4.6. One atmosphere vesiculation

The bubble sizes in our experiments are all much smaller than those commonly found to follow power-law distributions in natural and analogue rocks. The bubble sizes which follow a power law in the Etna lavas studied by Gaonac'h et al. (1996a) often have a minimum cut-off area of 10^5 μm^2; this size is greater than the maximum area of bubbles measured in our experiments. To evaluate the possibility that our bubbles sizes were too small to create a power-law distribution, we performed the 1 atm experiment, AB-24, in which all 10.9 wt.% of the water exsolved and formed bubbles.

The bubble sizes in AB-24 span a similar range as in the high-pressure experiments, but in contrast to the high pressure experiments in which only a small amount of water exsolved, the bubble-size distribution in the 1 atm. experiment follows a power law with an exponent of ~0.9 (Fig. 12a). Many large bubbles are found in this experiment and its texture closely resembles that of a pumice (Fig. 12b). The bubbles in this experiment are not spherical, as seen for all other experiments, but instead their shapes are influenced and distorted by neighboring bubbles and bubble coalescence is common. Experiment AB-24's power-law bubble-size distribution formed at far-from-equilibrium conditions and bubble growth abruptly stopped when the water diffusion coefficient became too low and the melt viscosity too high for bubble growth. This behavior implies that power-law distributions of bubble sizes are transient phenomena.

5. Discussion

5.1. Single-step decompression experiments at 450 MPa, 1200 °C

The single-step decompression experiments performed at 450 MPa, 1200 °C demonstrate that portions of the bubble-size distributions may be described by power laws for the zero-time and 0.5 h experiments, but that experiments of longer duration are better described by exponential distributions. The experiments demonstrate the rapid evolution of the bubble-size distribution and are consistent with our expectations based upon the model of Gaonac'h

et al. (1996b), in which a bubble-size distribution with an exponent near 1 evolves to a higher exponent with time. We are surprised, however, by the rapidity at which the evolution occurs, and that by 2 h the bubble sizes are better characterized by exponential distributions rather than power law ones.

The evolution from a power law to an exponential distribution occurs through the growth of the large bubbles. This is most clearly seen by comparing the probability of finding a bubble with an area greater than 100 μm^2 (Figs. 2–6); for the zero-time experiments this probability is less than 0.0001, but rises to ~0.0001–0.02 by 0.5 h, 0.04–0.06 by 2 h, 0.08–0.2 by 8 h, and 0.3 after 32 h. These results demonstrate that larger bubble sizes are becoming more common, while at the same time the vesicularities of the samples, which average $6.8 \pm 0.8\%$, are not changing significantly (Table 2). The absence of a significant change in vesicularities while larger bubbles are becoming more common as the experimental duration increases suggests a mechanism by which large bubbles grow at the expense of small bubbles, rather than the formation of new bubbles or continued growth of pre-existing bubbles by further exsolution of water from the melt.

The results of these experiments allow us to rule out a number of hypothesized growth mechanisms. The experimental bubble-size distributions in experiments longer than 0.5 h are best characterized by exponential functions. The value of the B parameter in the exponential equation (Eq. (1).) varies from 0.015 to 0.035, more than a factor of 2, and does not display a clear dependence with experimental duration. Although an exponential distribution of bubble sizes has been observed in natural rocks and is predicted by Cashman and Mangan (1994), their model does not seem applicable because our experiments are not at steady state conditions, as exemplified by the time dependence of the probability of finding bubbles with an area greater than 100 μm^2 and as reflected by the inconstancy of the B parameter.

Two other mechanisms for bubble growth also do not appear applicable to these experiments. Growth from differing sized "basins of attraction" (Buldyrev et al., 2003) should not only result in a power-law distribution, but also produce constant relative probabilities of the larger and smaller bubbles; because we do not observe a power law in the longer duration experiments, nor do the relative probabilities of the different bubble sizes remain constant in experiments of differing duration, this mechanism appears unlikely. Although a mechanism of continuous nucleation and growth can result in a bubble-size distribution similar to what we observe (Blower et al., 2001, 2002), our observations argue against this mechanism because such a process will produce larger vesicularities with increasing experimental duration, which we do not see. We conclude that the growth of the larger bubbles occurs at the expense of the smaller bubbles.

Two mechanisms may be responsible for the growth of large bubbles at the expense of small ones. One mechanism for this process is the coalescence of small bubbles to make larger ones, which is supported by the occasional observation of bubbles undergoing coalescence in the experiments (Fig. 1c). Another mechanism is Ostwald ripening; this process is the result of the relatively large contribution of the surface free energy to the total free energy of small phases which requires greater supersaturation at the interface of small phases than of large phases. The concentration difference between the interfaces of large and small phases creates a chemical potential gradient which drives diffusion from the smaller phases to the larger ones resulting in diminution of the former and growth of the latter (for more information see Lasaga, 1998; p. 515); in these experiments the rate of this process is controlled by diffusion of H_2O in the melt between the smaller and larger bubbles.

Although both processes contribute to the bubble-size distributions measured in the experiments, comparison of the bubble growth models reviewed above demonstrates that the most appropriate model to describe the results at 1200 °C, 450 MPa is that proposed by Gaonac'h et al. (1996b). The shorter duration experiments demonstrate power laws with exponents similar to those predicted by Gaonac'h et al. (1996b), which with increasing experimental duration evolve to exponential distributions. As the supply of small bubbles, which coalesce to form larger ones, is depleted the system enters the "decaying coalescence regime" (Gaonac'h et al., 1996a,b) and the bubble-size distribution may be described by an exponential function. Importantly, the finding of an exponential distribution of bubble sizes does not eliminate the possible role of coalescence in the growth of larger bubbles.

The presence of exponential bubble-size distributions in the longer duration experiments is not unexpected when compared to the results of most previous experimental studies of bubble growth due to water exsolution from silicate melts. Virtually all of these studies found Gaussian distributions of bubble sizes (e.g. Lyakhovsky et al., 1996; Navon and Lyakhovsky, 1998; Gardner et al., 1999; Mourtada-Bonnefoi and Laporte, 2002; Larsen et al., 2004; Mangan et al., 2004), similar in functional form to the exponential bubble-size distributions found in the longer duration experiments of this study.

One exception to the finding of exponential bubble-size distributions is the study of Simakin et al. (1999). These authors performed 7 experiments in which a granitic melt was continuously degassed with concurrent crystallization. The experimental pressures varied from 450 to approximately 40 MPa and experimental durations were typically 168 h. Most of the bubble-size distributions in their experiments were exponential, but the two that degassed approximately 4 wt.% H_2O during continuous decompression and underwent substantial crystallization in the presence of feldspar seeds display a power-law size distribution of bubbles. These experiments are characterized by the highest vesicularities produced in their study, 62% and 52%, and the crystallinity of these experiments is 30–40% (Simakin et al., 1999). The power-law bubble-size distribution found

in these experiments by Simakin et al. (1999) appears related to the concomitant bubble growth and crystallization which virtually filled the capsule with bubbles and crystals, possibly creating an example of Apollonian or closest packing (Blower et al., 2002; Dodds and Weitz, 2002).

5.2. Single-step decompression experiments at 450 MPa, 800 °C

One of the distinguishing characteristics of the 800 °C experiments is the smaller bubble size compared to those formed at 1200 °C; most bubbles are less than 20 μm^2, and the probability of finding a larger bubble is less than approximately 0.01 in both the 2 and 32 h experiments. This observation demonstrates that an increase in the experimental duration by a factor of 16 does not affect the distribution of the small bubbles at 800 °C, and even the probability distribution of the rare bubbles up to 1000 μm^2 size does not change significantly with time. Although power laws with exponents increasing from an average of ~2.1 at 2 h to ~2.6 at 32 h can describe the size distributions for bubbles between 4 and 20 μm^2, the distributions for bubbles up to 20 μm^2 are excellently fit by exponentials, which are characterized by B values (see Eq. (1)) that only vary from 0.227 to 0.256, or a difference of less than 13 relative percent.

With the exception of AB-21, whose vesicularity is anomalously low, the average vesicularity of the other three experiments at 800 °C, 450 MPa is $4.5 \pm 0.2\%$, or approximately 2.3% lower than the average of experiments at 1200 °C and 450 MPa, even though the solubility of water in albite melt is virtually temperature independent at 450 MPa (Behrens et al., 2001). The difference of 2.3% in vesicularity can be explained by the differing molar volumes of H_2O at 1200 and 800 °C, 450 MPa; the molar volume of H_2O at 450 MPa decreases from 3.62×10^{-5} m^3 at 1200 °C to 2.71×10^{-5} m^3 at 800 °C (calculated following Duan et al., 1992), or by a factor of 0.75×. This change in the molar volume of water is similar to the factor of 0.67× decrease between the average vesicularities measured in experiments performed at 1200 and 800 °C and accounts for this difference between the experiments.

Although the change in the molar volume of water provides an adequate explanation for the differing vesicularity of the two sets of experiments, it does not explain the difference in their bubble-size distributions. If the difference in the molar volume of H_2O between the high- and low-temperature experiments is applied to the size of individual bubbles, decreasing the temperature from 1200 to 800 °C at 450 MPa only reduces individual bubble areas by less than 30 relative percent, which is much smaller than the difference between the bubble sizes in these two sets of experiments. Thus, whereas the molar volume of water controls the difference in the bulk vesicularities of experiments at 800 and 1200 °C, 450 MPa, it does not control the difference between the bubble-size distributions seen in these experiments.

The differences between the bubble-size distributions observed in the 1200 and 800 °C experiments are attributable to the effects of temperature on water diffusion and melt viscosity (e.g. Scriven, 1959; Sparks, 1978; Toramaru, 1989, 1995; Proussevitch et al., 1993; Sparks et al., 1994; Proussevitch and Sahagian, 1998; Navon and Lyakhovsky, 1998; Lensky et al., 2004; Yamada et al., 2005). Proussevitch et al. (1993) modeled the effects of varying the water diffusivity and melt viscosity on bubble growth at isothermal, isobaric conditions. These authors performed computer simulations of bubble growth in rhyolitic and basaltic melts with water diffusion coefficients varying from 10^{-14} to 10^{-6} $m^2\,s^{-1}$ and melt viscosities from 10^1 to 10^7 Pa s. They found that the diffusion coefficient of water significantly affected the bubble growth rate such that when water diffuses at 10^{-13} $m^2\,s^{-1}$ (similar to the diffusivity of H_2O in our 800 °C experiments) the time necessary to reach the final bubble size was approximately 10000 s (~3 h) in their simulations, whereas a diffusion coefficient of 10^{-11} $m^2\,s^{-1}$ (similar to our 1200 °C experiments) yielded a simulation time of only 200 s to reach the final volume (Proussevitch et al., 1993). Their results also demonstrated that at viscosities of 10^3–10^4 Pa s there was no significant influence of melt viscosity on the bubble growth rate in rhyolitic melts and at viscosities between 10^1 and 5×10^3 Pa s there was no affect in basaltic melts (Proussevitch et al., 1993). The viscosities of hydrous albite melts at high pressures vary from 20 Pa s, at 1200 °C, to 9000 Pa s at 800 °C, and span the range in which viscosity is expected to have no significant affect on bubble growth rates. We might conclude that the differences between the bubble size distributions formed in the 1200 and 800 °C experiments are due solely to the reduction in the water diffusion coefficient at lower temperature. However, before entirely eliminating viscosity as an important control on bubble size we need to consider its affect on bubble–bubble interactions.

An important difference between our experiments and bubble growth simulations is that bubbles in our capsules can move and coalesce. Although the differences in melt viscosity at 800 and 1200 °C may have no significant effect on the growth of individual bubbles, these differences can significantly influence possible interactions between bubbles. The bubbles in our experiments can move by two mechanisms and as they move a bubble may "sweep up" other bubbles by coalescence. The first transport mechanism is Brownian motion which can be calculated by the expression:

$$x = \sqrt{2Dt}, \tag{3}$$

where x is the transport distance, D is the diffusion coefficient, and t is the time (Einstein, 1905). The diffusion coefficient for the bubbles in Eq. (3) is calculated from the Stokes–Einstein diffusion relation

$$D = \frac{kT}{6\pi r\eta}, \tag{4}$$

where k is Boltzmann's constant, T is the temperature in Kelvins, r is the radius of the bubble, and η is the melt viscosity (Einstein, 1905). The second mechanism is ascent of the less-dense bubbles through the more-dense melt, which is calculated by Stokes' law:

$$v = \frac{2\Delta\rho g r^2}{9\eta}, \quad (5)$$

where v is the ascent velocity, $\Delta\rho$ is the density difference between the melt and the fluid, and g is Earth's gravity. At 450 MPa, 1200 °C the melt density is 1.95×10^3 kg m^{-2} (Ochs and Lange, 1997), the water fluid density is 4.98×10^2 kg m^{-2} (Duan et al., 1992); g is 9.8 m s^{-2}, and the melt viscosity is 20 Pa s (Dingwell, 1987). At 450 MPa, 800 °C the melt density is 2.08×10^3 kg m^{-2}, the water fluid density is 6.64×10^2 kg m^{-2}, and the melt viscosity is 9000 Pa s.

Considering a bubble of 1 μm radius, at 1200 °C its transport by Brownian motion in 1 s would be 10^{-8} m and at 800 °C it would be 10^{-10} m. Whereas, the ascent rate of the same bubble by Stokes' law at 1200 °C is 10^{-10} m s^{-1} and at 800 °C is 10^{-13} m s^{-1}. In an 8 h experiment the transport distance by Brownian motion is 2 μm at 1200 °C and 0.1 μm at 800 °C, whereas Stokes' equation predicts ascents of 5 μm and 0.01 μm at the same temperatures, respectively. Extending these calculations we consider the behavior of the largest bubbles, with radii of ~30 μm, in an 8 h duration experiment. For this case, Brownian motion results in transport of only 0.3 μm at 1200 °C and 0.01 μm at 800 °C. Whereas in 8 h the Stokes' law ascents are 9 μm at 800 °C and 4 mm at 1200 °C. Both the diffusive and the density driven transport mechanisms are far more rapid in the higher temperature melts and subsequently the probability for bubble coalescence is significantly enhanced in the higher temperature experiments, thus explaining the larger bubbles found in the higher temperature experiments.

However, the 800 °C experiments consistently generated a small population of large bubbles, reaching at least 1000 μm^2. These rare, large bubbles are most probably formed by the coalescence of smaller bubbles which originally nucleated close together, but these larger bubbles are rare because of the higher viscosity and shorter bubble transport distances in the 800 °C melt.

Thus, in addition to changes in water diffusion with temperature, melt viscosity is responsible for the differences in the bubble-size distributions between the 1200 and 800 °C experiments because of the viscosity effect on bubble transport and thus on the probability of coalescence. This probability increases dramatically when bubble size reaches the 20 μm^2 size class, approximately equivalent to a radius of 2.5 μm, and Stokes' ascent becomes rapid. Thus, in these experiments the diffusive regime for bubble growth as defined by Gaonac'h et al. (1996a,b) extends to bubbles of approximately 20 μm^2, and larger bubbles grow dominantly by coalescence, even when the vesicularity is low. The inferred transition from the diffusive to the coalescence growth regime at ~20 μm^2 in these experiments compares favorably to the similar transition in natural pumices observed at ~50 μm^2 by Gaonac'h et al. (2005).

5.3. Single-step decompression to 400 MPa at 1200 °C

Experiments AB-27 and AB-29 were performed for comparison with the multiple-step decompression experiments discussed below. The probability of finding a bubble with an area greater 100 μm^2 is approximately 0.01 in both of these 1200 °C, 400 MPa experiments, which were of 2 and 8 h duration (Figs. 9 and 10). The vesicularity of these experiments should be larger than those at 450 MPa because of the approximately 3× mass of exsolved water and the larger molar volume of water at 400 MPa; combining the molar volume of water at 400 MPa, 3.89×10^{-5} m^3 mol^{-1}, and at 450 MPa 3.62×10^{-5} m^3 mol^{-1} (Duan et al., 1992), with the additional exsolved water at 450 MPa leads to the prediction of a 400 MPa vesicularity that is 60% greater than at 450 MPa. Such a high vesicularity was not measured in the images used for measuring bubbles (Table 2), however the large bubbles along the edges of the capsule were not considered in our analysis and these bubbles are voluminous enough to explain the discrepancy between the measured and expected vesicularities. One example of this "missing" vesicularity is seen in an image of AB-29 that has a large bubble adhering to the capsule wall. When this large bubble is counted the vesicularity is 12%, but when it is ignored the vesicularity drops to only 4%. These large bubbles play a significant role in determining the vesicularity of an experiment or a rock (c.f. Gaonac'h et al., 1996a,b), but, as discussed previously, these bubbles are rare, difficult to measure accurately, and quite possibly produced by heterogeneous nucleation on the capsule walls. Therefore they were deliberately not incorporated into the results of this study.

The similarity of the bubble distributions measured in experiments performed at 450 and 400 MPa indicates that the same process occurs at both conditions: larger bubbles grow at the expense of smaller bubbles and that the difference in the amount of exsolved water, ~0.5 wt.% at 450 MPa and ~1.5 wt.% at 400 MPa, does not affect the bubble growth mechanism.

5.4. Two-step decompression experiments to 400 MPa at 1200 °C

These two-step experiments demonstrate that the decompression path has only a small effect on the bubble-size distribution. The bubble sizes in the 8 h two-step experiments at 400 MPa are very similar to those in the single-step experiments at 450 MPa (Fig. 11), as is the vesicularity in all 400 MPa experiments, despite the ~3× larger amount of water exsolved in the lower pressure experiments. The large bubbles and "missing" vesicularity also can be found in the large bubbles adhering to the inner walls of the capsule (discussed previously).

The similarity of the bubble-size distributions in the single-step and two-step experiments indicates that the two-step decompression experiments may create slightly larger bubbles than single-step experiments. Importantly, we found no evidence of multiple nucleation events, which are expected to affect the bubble-size distribution (Blower et al., 2001, 2002). Therefore, the mechanisms of bubble size evolution in both single- and two-step experiments appear identical.

5.5. Evolution of bubble radii with time

The bubble areas were converted into three-dimensional bubble radii distributions to investigate the growth of bubble radii with time (Fig. 13). After eliminating the small bubbles formed during quenching, these distributions were fit with a Gaussian function to calculate the mean bubble radius and 1-sigma standard deviation (Table 2, Fig. 14). In some cases the distribution is excellently fit by Gaussian function (e.g., AB-15), however in other cases the fit is not very good (AB-27), and in two cases the data could not be fit properly (AB-20, AB-24) and produced an average radius less than zero. These variations reflect the complexity of the bubble-size distributions in the experiments and serve as a reminder that a single-valued descriptor of the bubble sizes, such as the mean radius, is only a gross description of the bubbles. Despite this caveat, the mean bubble radii display important trends with time that provide insight into bubble growth mechanisms. For times up to 2 h (7200 s) at 450 MPa, 1200 °C, the mean radii of the bubbles can be fit with an exponential function, but when all experiments at this pressure and temperature are considered the mean bubble radii follow a power-law relationship with time, with an exponent of 0.35.

Bubble growth in short duration experiments appears to follow an exponential law, as proposed by Toramaru

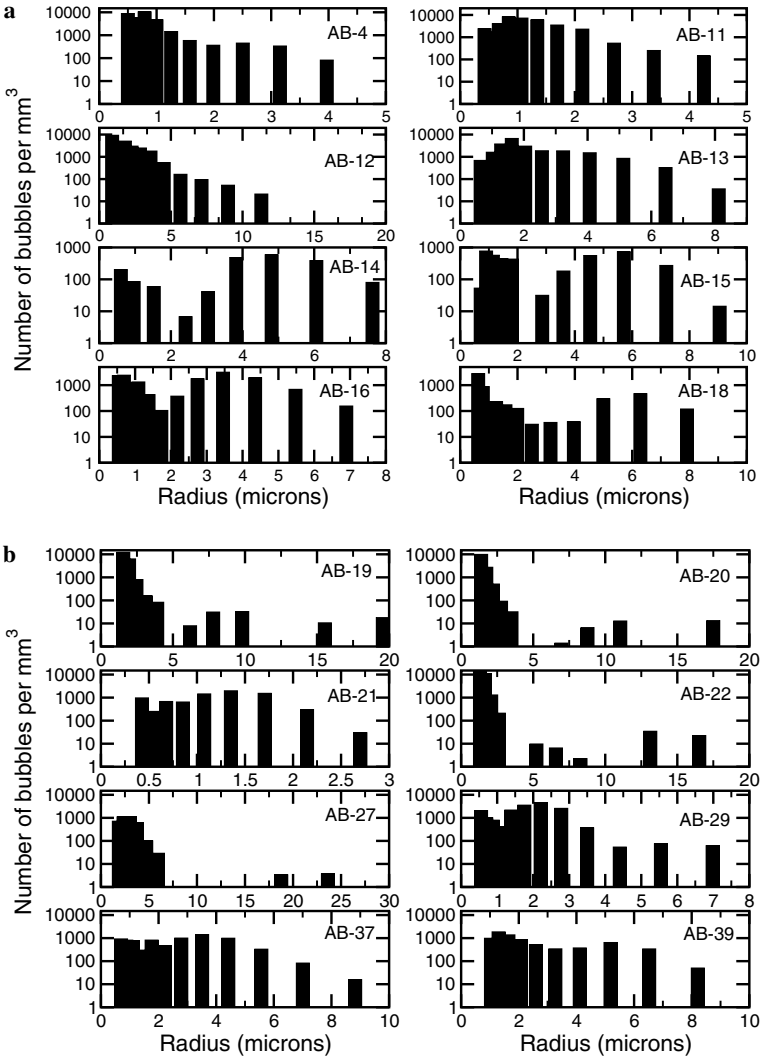

Fig. 13. Three-dimensional bubble radii distributions calculated from the two-dimensional measurements using the techniques of Sahagian and Proussevitch (1998). (a) All single-step decompression experiments at 1200 °C, 450 MPa. (b) Single-step decompression experiments at 800 °C, 450 MPa, AB-19 through AB-22; single-step decompression experiments at 1200 °C, 400 MPa, AB-27 and AB-29, and two-step decompression experiments at 1200 °C, 400 MPa, AB-37 and AB-38.

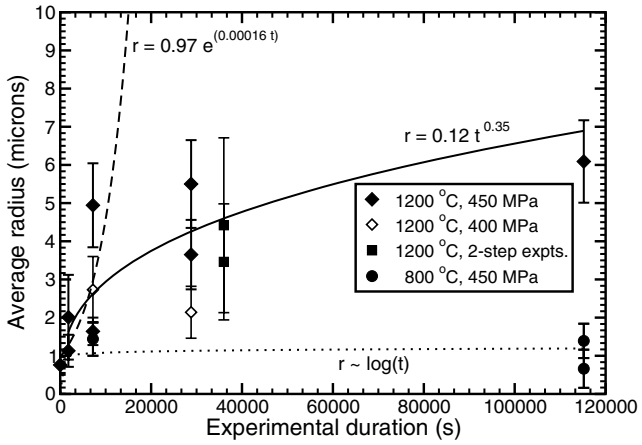

Fig. 14. Average bubble radii as a function of time. Average radii and 1-sigma standard deviations were calculated by fitting a Gaussian distribution to the data in Fig. 13, but ignoring the small bubbles formed during quenching. The data from the single-step decompression experiments at 450 MPa, 1200 °C with durations of 0 and 1800 s (0.5 h) have been fit with an exponential function and experiments of 1800–111500 s (32 h) have been fit with a power-law function. The measured radii from all 1200 °C experiments in this study are consistent with the power-law function whose exponent is 0.35, very close to the theoretical value of 1/3 for Ostwald ripening. The 800 °C experiments display smaller radii that are approximately time invariant. However, these data can be fit with a log function reminiscent of that empirically discovered by Proussevitch and Sahagian (1998) in their bubble growth simulations for rhyolitic magmas.

(1995) and Navon and Lyakhovsky (1998) for early-stage bubble growth in the viscosity controlled regime. This agreement appears fortuitous when the numerical values in the fit are compared with the proposed growth equation. The equation describing exponential bubble growth during the initial stages when the surface area to volume ratio of the bubble is large and diffusion of volatiles into the bubble is rapid enough to maintain the gas pressure in the bubble close to the value at the point of nucleation is:

$$r \propto \exp\left[\frac{\Delta P}{4\eta}t\right], \tag{6}$$

where r is the bubble radius, ΔP is the difference between the volatile pressure inside the bubble and the ambient pressure, η, is the melt viscosity, and t is the time. The applicability of this relationship to the experiments of this study can be tested by comparing the melt viscosity calculated from this equation with the known viscosity of the melt. Estimating ΔP to be 25 MPa, the exponential fit to the data predicts a melt viscosity of $\sim 4 \times 10^4$ Pa s, far above the 20 Pa s viscosity at 1200 °C (Dingwell, 1987). This large discrepancy indicates that the exponential growth stage ends in less than 0.5 h after bubble formation in this system.

The power-law function was fit only to the single-step, bubble growth experiments at 1200 °C, 450 MPa, but both the single-step experiments at 1200 °C, 400 MPa and the two-step experiments at 1200 °C are consistent with the function (Fig. 14). One of the experiments at 400 MPa, AB-27 of 2 h duration, displays a mean radius which is consistent with the 450 MPa growth rate, but the other 400 MPa experiment, AB-29 of 8 h duration, has an anomalously small average radius. Such anomalies appear inherent in these experiments in which stochastic processes play an important role and are also exemplified by the variations in the mean bubble radii in the 2 and 8 h experiments at 1200 °C and 450 MPa (Fig. 14). Despite the variations, these data lead us to conclude that the growth in bubble radii with time is best described by a power-law function for experiments at 400 and 450 MPa, 1200 °C.

The exponent of the power-law fit to the bubble radii in the 1200 °C experiments, 0.35, is similar to the theoretical exponent for Ostwald ripening, 1/3, as deduced by Lifshitz and Slyozov (1961) and extended to liquid systems in which coalescence occurs by Binder and Stauffer (1974) and Siggia (1979). A simple derivation of the power law exponent of 1/3rd for Ostwald ripening can be constructed following Bray (2002), who used the Stokes–Einstein relationship to show that the time it takes for a "particle" to be transported over a distance which is a multiple of its radius r, or xr, is (c.f., Eq. (3))

$$t \approx \frac{x^2 r^2}{D}, \tag{7}$$

and with the substitution of D from Eq. (4)

$$t \approx \frac{6\pi\eta x^2 r^3}{kT}, \tag{8}$$

which when rearranged yields the appropriate power-law scaling relationship

$$r(t) \approx \left[\frac{kT}{6\pi\eta x^2}\right]^{\frac{1}{3}} t^{\frac{1}{3}}. \tag{9}$$

The close correspondence between the exponent for the growth of the mean bubble radii determined in these experiments and theories of phase segregation and growth in fluids involving Ostwald ripening suggests that this is the dominant process for the growth of most bubbles in the experiments. However, other growth mechanisms may be operating in these experiments, especially for the larger bubbles; for example, transport of the larger bubbles in the experiments is dominated Stokes' ascent which should lead to a linear relationship between the radii and t (Bray, 2002). But these bubbles are typically a small proportion of those found in most the experiments (Fig. 13) and their contribution to the mean radius for each experiment is overwhelmed by the more-numerous, small bubbles. However, the observation that the measured power-law exponent is slightly above the theoretical one may reflect the operation of other processes in the experiments.

As discussed previously, the smaller average bubble sizes in the 800 °C experiments are due to the orders of magnitude higher melt viscosity and orders of magnitude lower water diffusion coefficients than in the 1200 °C experiments. The scaling equation for Ostwald ripening (Eq. (9)) suggests that the differences between the melt properties at the two temperatures studied should lead to a

growth rate at 800 °C which is ~1/8 the rate at 1200 °C. Thus we would expect the radii of the 2 h experiments at 800 °C, ~1.4 μm, to be similar to the calculated radius of bubbles grown for 0.25 h at 1200 °C, or 1.3 μm. The success of this argument is tempered by the observation that the bubble radii in the 32 h experiments at 800 °C are no larger than in the 2 h experiment.

The lack of bubble growth between 2 and 32 h does not reflect the attainment of the equilibrium bubble radius in the 2 h experiments. We can demonstrate this by calculation of the final, equilibrium, bubble radius, r_f, using the relationship given in Navon and Lyakhovsky (1998)

$$r_f^3 = S^3(C_o - C_f)\frac{\rho_m}{\rho_f}, \quad (10)$$

where S is the average distance between the bubbles (Table 2), C_o is the initial and C_f is the final water concentration in the melt, ρ_m is the melt density and ρ_f is the water fluid density. Given an average S of 30 μm (Table 2), the melt and fluid densities (discussed above) and a concentration difference of 0.5 wt.%, the r_f at 800 °C is 7.5 μm and at 1200 °C is 8.1 μm. Thus although the 1200 °C bubbles are near their equilibrium radius, the 800 °C bubbles are not and thus the small, almost time independent, bubble sizes seen in these experiments are not an equilibrium phenomenon, but most probably are due to the bubble growth mechanisms.

The discrepancy between the 800 °C results and the power-law model for bubble growth suggests the possibility of a different growth law in these lower-temperature experiments. One possible growth law is that empirically discovered by Proussevitch and Sahagian (1998) in their simulations of bubble growth in a high-viscosity, low water-diffusivity, rhyolitic melt

$$r \approx \log(t). \quad (11)$$

The bubble radii measured in the 800 °C experiments can be fit with such a growth law (Fig. 14), if one assumes the presence of nanoscale bubble nuclei at zero time (Mangan and Sisson, 2000). However, not even the newest theoretical models for bubble formation and growth in magmatic systems (e.g. Lensky et al., 2004; Yamada et al., 2005) have found such a relationship and its exact origin is unclear. We attribute the differences in the bubble growth laws at 1200 and 800 °C to the higher viscosity and lower diffusion in the 800 °C melts, but cannot eliminate the possible influence of different bubble-melt surface free energies at the two temperatures because their values are unknown.

5.6. Application to igneous processes

The viscosities and water diffusion coefficients of albite melt in the 1200 °C experiments, 20 Pa s and ~ 5×10^{-11} m^2 s^{-1}, respectively, are similar to those of basaltic melts, whereas in the 800 °C experiments these properties, 9000 Pa s and ~2×10^{-13} m^2 s^{-1}, respectively, resemble those of hydrous andesitic to dacitic melts (c.f. Proussevitch et al., 1993). Thus, the results of this study provide insight into exsolution of small amounts of water from melt compositions ranging from mafic to intermediate.

At all experimental conditions bubble nucleation occurred without measurable delay, even though the amount of water exsolved was only ~0.5 to 1.5 wt.%, corresponding to supersaturation pressures of 25–75 MPa. The bubble number densities of this study (Table 2) are not correlated with temperature and are similar to those measured in previous studies of rhyolitic melts, often created at larger supersaturation pressures (e.g. Hurwitz and Navon, 1994; Lyakhovsky et al., 1996; Gardner et al., 1999; Mangan and Sisson, 2000; Larsen and Gardner, 2000; Mourtada-Bonnefoi and Laporte, 2002, 2004; Larsen et al., 2004). The ease and rapidity of nucleation in these experiments reinforces the findings of previous studies indicating that delayed nucleation is only expected to occur in high viscosity rhyolitic melts at similar supersaturation pressures (e.g. Hurwitz and Navon, 1994; Lyakhovsky et al., 1996; Gardner et al., 1999; Larsen and Gardner, 2000; Mangan and Sisson, 2000; Mourtada-Bonnefoi and Laporte, 2002, 2004; Larsen et al., 2004). Magmas ranging in composition from basaltic to dacitic will be able to nucleate and grow bubbles with as little as 25 MPa supersaturation pressure. Most mafic magmas ascend through the crust at velocities one or two orders of magnitude below the ~1 MPa s^{-1}, or ~33 m s^{-1}, decompression rate of used in this study (e.g. Alletti et al., 2005). Therefore, virtually all ascending mafic magmas are expected to rapidly nucleate bubbles even when only supersaturated by 0.5 wt.% H_2O, and significant supersaturation in these melts, which could potentially lead to plinian eruptions, is not expected unless the decompression rate is extremely rapid.

Mafic and intermediate melts supersaturated by only small amounts of water at constant pressure will nucleate bubbles rapidly, but the growth rates of the bubbles in the two melts will be significantly different. Bubbles growing from slightly supersaturated mafic melts at constant pressure will reach near-equilibrium dimensions in approximately 2 days due to their power-law growth, whereas bubbles in high-viscosity, intermediate-to-silicic melts may take weeks to months because of their logarithmic dependence upon time. The high bubble growth rates from mafic melts result in the bubbles rapidly growing large enough that transport due to density differences between the bubbles and the melt following Stokes' law quickly becomes important. Rapid ascent of bubbles by this mechanism greatly enhances the probability of bubble coalescence creating even larger bubbles, which ascend more quickly, and possibly result in foam formation, which conceivably could separate from the rest of the magma. The slower growth of bubbles expected in intermediate-composition melts indicates that there will be a long hiatus between the formation of most bubbles and growth to sizes where ascent follows Stokes' law. In this case coalescence

should be less efficient and there is little possibility of foam formation and separation. Thus the separation of bubbles from intermediate melts will be much less efficient than from mafic ones. However, the 800 °C experiments consistently produced a small number of large bubbles. These large bubbles can ascend by Stokes' law and more efficiently coalesce, suggesting the possibility that a bimodal size distribution of bubbles, small and large, may develop in intermediate melt compositions. Bimodal bubble-size distributions have been observed in natural pyroclasts and previously attributed to multiple nucleation events (e.g. Formenti and Druitt, 2003 and references therein), but our results indicate the possibility of developing a bimodal bubble-size distribution with only one nucleation event during the exsolution of only small amounts of water in intermediate-composition melts.

The bubble-size distributions formed by the exsolution of small amounts of water rapidly evolve from ones described by power-law functions into ones described by exponentials. This evolution of the distributions occurs in the space of only a few hours. The finding of power-law bubble-size distributions in natural rocks that contain less than 10 volume percent of bubbles indicates that the time between the formation of the bubbles and their quenching is less than a few hours. This observation suggests that a power-law bubble-size distribution may possibly be used as a geospeedometer capable of constraining the time between bubble formation and quenching of the sample.

Acknowledgments

This research presents the results the B.Sc. research project of J.-F. Bergevin and P. Lang, an NSERC USRA and undergraduate research course of G. Robert and CEGEP summer internship of E. Allard. This paper benefited from the thorough reviews by an anonymous reviewer, A. Proussevitch and Associate Editor J. Rustad. Discussions with G. Paul, S. Sreenivasan, and S. Buldyrev on the topics of growth and power laws were much appreciated. Lang Shi is thanked for his help on the electron microprobe and Steve Kecani is thanked for his careful machining that keeps the lab operational. This research was financially supported by an NSERC Discovery Grant to D.R. Baker.

Associate editor: James R. Rustad

References

Abramoff, M.D., Magelhaes, P.J., Ram, S.J., 2004. Image processing with ImageJ. *Biophotonics Inter.* **11**, 36–42.

Alletti, M., Pompilio, M., Rotolo, S.G., 2005. Mafic and ultramafic enclaves in Ustica Island lavas: inferences on composition of lower crust and deep magmatic processes. *Lithos* **84**, 151–167.

Baker, D.R., 2004. Piston cylinder calibration at 400 to 500 MPa: a comparison of using water solubility in albite melt and NaCl melting. *Am. Mineral.* **89**, 1553–1556.

Behrens, H., Nowak, M., 1997. The mechanisms of water diffusion in polymerized silicate melts. *Contrib. Mineral. Petrol.* **126**, 377–385.

Behrens, H., Meyer, M., Holtz, F., Benne, D., Nowak, M., 2001. The effect of alkali ionic radius, temperature, and pressure on the solubility of water in $MAlSi_3O_8$ melts (M = Li, Na, K, Rb). *Chem. Geol.* **174**, 275–289.

Binder, K., Stauffer, D., 1974. Theory for the slowing down of the relaxation and spinodal decomposition of binary mixures. *Phys. Rev. Lett.* **33**, 1006–1009.

Blower, J.D., Keating, J.P., Mader, H.M., Phillips, J.C., 2001. Inferring volcanic degassing processes from vesicle size distributions. *Geophys. Res. Lett.* **28**, 347–350.

Blower, J.D., Keating, J.P., Mader, H.M., Phillips, J.C., 2002. The evolution of bubble size distribution in volcanic eruptions. *J. Volcanol. Geotherm. Res.* **120**, 1–23.

Bohlen, S.R., 1984. Equilibria for precise pressure calibration and a frictionless furnace assembly for the piston-cylinder apparatus. *N. Jahrbuch Mineral. Monat.* **9**, 404–412.

Bray, A.J., 2002. Theory of phase-ordering kinetics. *Adv. Phys.* **51**, 481–587.

Buldyrev, S.V., Dokholyan, N.V., Erramilli, S., Hong, M., Kim, J.Y., Malescio, G., Stanley, H.E., 2003. Hierarchy in social organization. *Physica A* **330**, 653–659.

Burgisser, A., Gardner, J.E., 2005. Experimental constraints on degassing and permeability in volcanic conduit flow. *Bull. Volcanol.* **67**, 42–56.

Cashman, K.V., Mangan, M.T., 1994. Physical aspects of magmatic degassing II. Constraints on vesiculation processes from textural studies of eruptive products. *Rev. Mineral. (Mineralogical Society of America, Washington)* **30**, 447–478.

Dingwell, D.B., 1987. Melt viscosities in the system $NaAlSi_3O_8$–H_2O–F_2O_{-1}. In: Mysen, B.O. (Ed.), *Magmatic Processes: Physicochemical Principles*. Geochemical Society Special Publication 1, University Park, pp. 423–431.

Dodds, P.S., Weitz, J.S., 2002. Packing-limited growth. *Phys. Rev. E* **65**, 056108.

Duan, Z., Møller, N., Weare, J.H., 1992. An equation of state for the CH_4-CO_2-H_2O system: I. Pure systems from 0 to 1000 °C and 0 to 8000 bar. *Geochim. Cosmochim. Acta* **56**, 2605–2617.

Einstein, A., 1905. Über die von der molekularkinetischen Theorie der Wärme geforderte Bewegung von in ruhenden Flüssigkeiten suspendierten Teilchen. *Ann. Phys.* **17**, 549–560 [Translated as: On the movement of small particles suspended in a stationary liquid demanded by molecular-kinetic theory of heat. In: Fürth, R. (Ed.), *Investigations on the Theory of the Brownian Movement by Albert Einstein* (A.D. Cowper, Transl.), Dover Publications, New York, 1956, pp. 1–18].

Formenti, Y., Druitt, T.H., 2003. Vesicle connectivity in pyroclasts and implications for the fluidisation of fountain-collapse pyroclastic flows, Montserrat (West Indies). *Earth Planet. Sci. Lett.* **214**, 561–574.

Gaonac'h, H., Stix, J., Lovejoy, S., 1996a. Scaling effects on vesicle shape, size and heterogeneity of lavas from Mount Etna. *J. Volcanol. Geotherm. Res.* **74**, 131–153.

Gaonac'h, H., Lovejoy, S., Stix, J., Scherzter, D., 1996b. A scaling growth model for bubbles in basaltic lava flows. *Earth Planet. Sci. Lett.* **139**, 395–409.

Gaonac'h, H., Lovejoy, S., Scherzter, D., 2005. Scaling vesicle distributions and volcanic eruptions. *Bull. Volcanol.* **67**, 357–360.

Gardner, J.E., Hilton, M., Carroll, M.R., 1999. Experimental constraints on degassing of magma: isothermal bubble growth during continuous decompression from high pressure. *Earth Planet. Sci. Lett.* **168**, 201–218.

Hergarten, S., 2002. *Self-Organized Criticality in Earth Systems*. Springer-Verlag, Berlin.

Hurwitz, S., Navon, O., 1994. Bubble nucleation in rhyolitic melts: experiments at high pressure, temperature, and water content. *Earth Planet. Sci. Lett.* **122**, 267–280.

Klug, C., Cashman, K.V., 1996. Vesiculation of May 18, 1980 Mount St. Helens magma. *Geology* **22**, 468–472.

Klug, C., Cashman, K.V., Bacon, C.R., 2002. Structure and physical characteristics of pumice from the climactic eruption of Mount Mazama (Crater Lake), Oregon. *Bull. Volcanol.* **64**, 486–501.

Larsen, J.F., Gardner, J.E., 2000. Experimental constraints on bubble interactions in rhyolite melts: implications for vesicle size distributions. *Earth Planet. Sci. Lett.* **180**, 201–214.

Larsen, J.F., Denis, M.-H., Gardner, J.E., 2004. Experimental study of bubble coalescence in rhyolitic and phonolitic melts. *Geochim. Cosmochim. Acta* **68**, 333–344.

Lasaga, A.C., 1998. *Kinetic Theory in the Earth Sciences*. Princeton University Press, Princeton.

Lensky, N.G., Navon, O., Lyakhovsky, V., 2004. Bubble growth during decompression of magma: experimental and theoretical investigation. *J. Volcanol. Geotherm. Res.* **129**, 7–22.

Lifshitz, I.M., Slyozov, V.V., 1961. The kinetics of precipitation from supersaturated solid solutions. *J. Phys. Chem. Solids* **19**, 35–50.

Lovejoy, S., Gaonac'h, H., Schertzer, D., 2004. Bubble distributions and dynamics: the expansion-coalescence equation. *J. Geophys. Res.* **109**, B11203. doi:10.1029/2003JB002823.

Lyakhovsky, V., Hurwitz, S., Navon, O., 1996. Bubble growth in rhyolitic melts: experimental and numerical investigation. *Bull. Volcanol.* **58**, 19–32.

Mader, H.M., Zhang, Y., Phillips, J.C., Sparks, R.S.J., Sturtevant, B., Stolper, E., 1994. Experimental simulations of explosive degassing of magma. *Nature* **372**, 85–88.

Mangan, M.T., Cashman, K.V., 1996. The structure of basaltic scoria and reticulite and inferences for vesiculation, foam formation, and fragmentation in lava fountains. *J. Volcanol. Geotherm. Res.* **73**, 1–18.

Mangan, M.T., Sisson, T., 2000. Delayed, disequilibrium degassing in rhyolite magma: decompression experiments and implications for explosive volcanism. *Earth Planet. Sci. Lett.* **183**, 441–455.

Mangan, M.T., Mastin, L., Sisson, T., 2004. Gas evolution in eruptive conduits: combining insights from high temperature and pressure decompression experiments with stead-state flow modeling. *J. Volcanol. Geotherm. Res.* **129**, 23–36.

Marsh, B.D., 1988. Crystal size distribution (CSD) in rocks and the kinetics and dynamics of crystallization. I. Theory. *Contrib. Mineral. Petrol.* **99**, 277–291.

Martel, C., Bureau, H., 2001. In situ high-pressure and high-temperature bubble growth in silicic melts. *Earth Planet. Sci. Lett.* **191**, 115–127.

Martel, C., Schmidt, B.C., 2003. Decompression experiments as an insight into ascent rates of silicic magmas. *Contrib. Mineral. Petrol.* **144**, 397–415.

Mourtada-Bonnefoi, C.C., Laporte, D., 2002. Homogeneous bubble nucleation in rhyolitic magmas: an experimental study of the effect of H_2O and CO_2. *J. Geophys. Res.* **107**, 2066, doi:10.1029/2001JB000290.

Mourtada-Bonnefoi, C.C., Laporte, D., 2004. Kinetics of bubble nucleation in a rhyolitic melt: an experimental study of the effect of ascent rate. *Earth Planet. Sci. Lett.* **218**, 521–537.

Navon, O., Lyakhovsky, V., 1998. Vesiculation processes in silicic magmas. In: Gilbert, J.S., Sparks, R.S.J. (Eds.), *The Physics of Explosive Volcanic Eruptions*. Geol. Soc. Spec. Publ., London, pp. 27–50.

Ochs, F.A., Lange, R.A., 1997. The partial molar volume, thermal expansivity, and compressibility of H_2O in $NaAlSi_3O_8$ liquid: new measurements and an internally consistent model. *Contrib. Mineral. Petrol.* **129**, 155–165.

Proussevitch, A.A., Sahagian, D.L., 1998. Dynamics and energetics of bubble growth in magmas: analytical formulation and numerical modeling. *J. Geophys. Res.* **103**, 18223–18251.

Proussevitch, A.A., Sahagian, D.L., Anderson, A.T., 1993. Dynamics of diffusive bubble growth in magmas: isothermal case. *J. Geophys. Res.* **98**, 22283–22307.

Rasband, W.S., 1997–2005. ImageJ, U.S. National Institutes of Health, Bethesda, Maryland, USA. Available from: <http://rsb.info.nih.gov/ij/>.

Sahagian, D.L., Proussevitch, A.A., 1998. 3D particle size distribution from 2D observations: stereology for natural applications. *J. Volcanol. Geotherm. Res.* **84**, 173–196.

Scriven, L.E., 1959. On the dynamics of phase growth. *Chem. Eng. Sci.* **10**, 1–13.

Shaw, H.R., 1974. Diffusion of H_2O in granitic liquids: Part I. Experimental data; Part II. Mass transfer in magma chambers. In: Hofmann, W., Giletti, B.J., Yoder, H.S., Jr.Jr., Yund, R.A. (Eds.), *Geochemical Transport and Kinetics*. Carnegie Institution, Washington, pp. 139–170.

Siggia, E.D., 1979. Late stages of spinodal decomposition in binary mixtures. *Phys. Rev. A* **20**, 595–605.

Simakin, A.G., Armienti, P., Epel'baum, M.B., 1999. Coupled degassing and crystallization: experimental study at continuous pressure drop, with application to volcanic bombs. *Bull. Volcanol.* **61**, 275–287.

Sparks, R.S.J., 1978. The dynamics of bubble formation and growth in magmas: a review and analysis. *J. Volcanol. Geotherm. Res.* **3**, 1–38.

Sparks, R.S.J., Barclay, J., Jaupart, C., Mader, H.M., Phillips, J.C., 1994. Physical aspects of magma degassing. I. Experimental and theoretical constraints on vesiculation. *Rev. Mineral. (Mineralogical Society of America, Washington)* **30**, 413–445.

Toramaru, A., 1989. Vesiculation process and bubble size distribution in ascending magmas with constant velocities. *J. Geophys. Res.* **94**, 17523–17542.

Toramaru, A., 1990. Measurement of bubble-size distributions in vesiculated rocks with implications for quantitative estimation of eruption processes. *J. Volcanol. Geotherm. Res.* **43**, 71–90.

Toramaru, A., 1995. Numerical study of nucleation and growth of bubbles in viscous magmas. *J. Geophys. Res.* **100**, 1913–1931.

Webb, S., Knoche, R., 1996. The glass-transition, structural relaxation and shear viscosity of silicate melts. *Chem. Geol.* **128**, 165–183.

Yamada, K., Tanaka, H., Nakazawa, K., Emori, H., 2005. A new theory of bubble formation in magma. *J. Geophys. Res.* **110**, B02203, doi:10.1029/2004JB003113.